UNIVERSITY OF OKLAHOMA

GRADUATE COLLEGE

DETERMINATION OF SHALE ANISOTROPIC POROVISCOELASTIC PROPERTIES FROM THREE-POINT BEAM BENDING TEST

A THESIS

SUBMITTED TO THE GRADUATE FACULTY

in partial fulfillment of the requirements for the

Degree of

MASTER OF SCIENCE

By

YANG ZHOU
Norman, Oklahoma
2017

Downloaded from SHAREOK. Persistent Handle URL: https://hdl.handle.net/11244/50861

DETERMINATION OF SHALE ANISOTROPIC POROVISCOELASTIC PROPERTIES FROM THREE-POINT BEAM BENDING TEST

A THESIS APPROVED FOR THE
MEWBOURNE SCHOOL OF PETROLEUM AND GEOLOGICAL ENGINEERING

BY

_____
Dr. Younane Abousleiman, Chair

_____
Dr. Ahmad Ghassemi

_____
Dr. Ahmad Jamili

© Copyright by YANG ZHOU 2017
All Rights Reserved.

Acknowledgements

I would first like to thank my thesis advisor Dr. Younane Abousleiman, Chair of the Integrated PoroMechanics Institute (iPMI) at the University of Oklahoma. He has always been a great mentor to me, providing me with insights and guiding me to think on my own whenever I ran into trouble writing my thesis or had a slight question about my research. Not only did he help me resolve my confusions on the reach, he was also consistently willing to go an extra mile by asking me more questions to encourage me to investigate further. Without his knowledge and experience, guide and assistance in the research I am involved in, I could have never initiated great passion in this program and gone this far in my research.

I would also like to dedicate my acknowledgement to Dr. Chao Liu, who has been providing me with tremendous help in finishing this thesis. His advanced mathematics knowledge was the key to solving some hardest questions I struggled with in deriving the analytical solutions. I am gratefully indebted to his every single piece of comment on my work. I cannot express my gratitude enough to Ms. Carla Cates as well for her assistance in arranging and organizing all the errands at iPMI to make everything run smoothly.

I would also like to recognize Dr. Ahmad Ghassemi and Dr. Ahmad Jamili for serving on my thesis committee. I could not have gone to this point and improved my thesis accordingly without their help and inputs.

Finally, I must express my profound gratitude to my parents for offering me unconditional support and continuous encourage for the past five years when I was away from home. They are the sole reason why I can focus on school and study what I am passionate about without worrying about anything else.

Table of Contents

Acknowledgements iv

Table of Contents v

List of Tables vii

List of Figures viii

Abstract xi

Chapter 1: Introduction 1

Chapter 2: Problem Description 7

2.1 Laboratory Set-up 7

2.2 Simulation 9

2.3 Initial and Boundary Conditions 12

Chapter 3: Governing Equations 15

3.1 Orthotropic Poroelasticity 15

3.2 Orthotropic Poroviscoelasticity 18

Chapter 4: Analytical Solutions 21

4.1 Poroelastic Solutions 21

4.2 Poroviscoelastic Solutions 24

Chapter 5: Numerical Examples 25

5.1 Effects of Anisotropy 29

5.2 Effects of Viscoelastic Properties 32

5.3 Effects of Various Shale Viscoelastic Behaviors 37

Chapter 6: Applications 39

6.1 Approximation of Shale Permeability 39

6.2 Sensitivity Studies 43

6.3 Potential Improvement of the Test 45

Chapter 7: Conclusions 47

References 48

Appendix A: Derivation of the Instantaneous Pore Pressure Jump 52

Appendix B: Poroelastic Solutions for Pore Pressure 55

Appendix C: Poroelastic Solutions for Moment and Load 59

List of Tables

Table 1. Initial and Boundary conditions in the simulation 12

Table 2. Mechanical properties of isotropic, transversely isotropic and orthotropic beam used in the simulation of the three-point beam bending test 28

List of Figures

Figure 1. CoreTest AP608 instrument used to measure porosity and permeability: time consuming for shale (OU IC3 Lab) 4

Figure 2. Pulse decay technique to measure rock permeability 4

Figure 3. Schematic of three-point beam bending test: the beam is bent to a constant deflection in the center and immersed in the liquid bath. 5

Figure 4. Free body diagram of the beam to which a force is applied in the three-point beam bending test 5

Figure 5. Thin section of the Woodford shale which reveals strong anisotropy (Sierra et al 2010). 6

Figure 6. Three-point beam bending test equipment (OU PoroMechanics Lab) 8

Figure 7. Placement of transversely isotropic beam: (a) measurement of permeability perpendicular to layers; (b) measurement of permeability parallel to layers 9

Figure 8. Cartesian coordinate for the three-point beam bending test throughout this work. The origin is in the center of the left most surface of the beam. 9

Figure 9. (a) Isotropic, (b) transversely isotropic, and (c) orthotropic materials encountered in this work and how their properties distinguish from each other. 11

Figure 10. Boundary conditions in the simulation: beam is sealed laterally at two far ends. Fluid can flow in only x and y direction. C stands for compression, T stands for tension. Δ is the deflection. 13

Figure 11. Schematic illustration of the bending of the beam under constant deflection when saturated with fluid. Fluid is squeezed out from the outer surface of the beam. .. 16

Figure 12. Schemetic representation of different viscoelastic models: (a) Kelvin model; (b) Maxwell model and (c) Zener model. 26

Figure 13. (a) The dimension and constant deflection of the beam in the three-point beam bending test simulation and (b) (c) (d) the definition of the mechanical properties in each direction: Young's Moduli and permeability in x, y and z direction are E_x, k_x, E_y, k_y, E_z and k_z respectively. 27

Figure 14. Poroelastic pore pressure distribution along x-axis at y=0mm and z=40mm at variable times for isotropic, transversely isotropic and orthotropic beams. 30

Figure 15. Poroelastic pore pressure distribution along y-axis at x=1mm and z=40mm at variable times for isotropic, transversely isotropic and orthotropic beams. 31

Figure 16. Poroelastic load decay to sustain a 1mm constant deflection for isotropic, transversely isotropic and orthotropic beams. 32

Figure 17. Poroelastic and poroviscoelastic pore pressure distribution along x-axis at y=0mm and z=40mm at variable times for transversely isotropic beam. 34

Figure 18. Poroelastic and poroviscoelastic pore pressure distribution along y-axis at x=1mm and z=40mm at variable times for transversely isotropic beam. 35

Figure 19. Poroelastic and poroviscoelastic load decay to sustain a 1mm constant deflection for transversely isotropic beam. 36

Figure 20. Poroviscoelastic load decay to sustain a 1mm constant deflection for orthotropic beams simulated by different viscoelastic models. 38

Figure 21. Simple work flow of determining which viscoelastic model to use based on the load decay data. 40

Figure 22. Experimental data of load decay of a shale under 1mm constant deflection three-point beam bending test. 42

Figure 23. Matching the analytical solution of the poroviscoelastic load decay to the experimental data to obtain the estimated permeability. 43

Figure 24. Poroviscoelastic load decay solutions with modified permeability 44

Figure 25. Poroviscoelastic load decay with modified viscoelastic parameter 45

Abstract

Permeability is an extremely important property of shale. It is essential to know permeability as it can aid engineers in developing drilling and production strategies and help executives make important financial decisions. However, the measurement of shale permeability has long been a challenge in the industry due to shale's extremely low porosity and permeability (in Nano Darcy range). Conventional method of measuring shale permeability may take hours even days. This work presents a new permeability measurement method named three-point beam bending test that was originally invented and developed by Scherer in 1992. This method approximates shale permeability that is in reasonable agreement with the theoretically predicted values from empirical equations.

In this thesis, orthotropic poroelastic solutions of the pore pressure and load decay are derived and studied. The thesis also extends the poroelastic solutions to poroviscoelastic solutions to accommodate the viscoelasticity of the shale.

Viscoelastic properties of shale complicate the problem, thus two viscoelastic models are introduced in this thesis. The analytical solutions pore pressure and load decay under constant deflection test are plotted and investigated. Influence of anisotropy, viscoelastic properties and sensitive of permeability on the solutions are studied. In practice, the permeability of the shale beam is approximated by matching the analytical solution of the load decay to the experimental data acquired from the constant deflection test.

At last, potential limitations of the experiment and improvements are discussed.

Chapter 1: Introduction

Shale has been a trending research focus in the petroleum industry and will continue to be investigated as techniques to produce from conventional resources have been studied thoroughly. Porosity and permeability are two essential factors to determine the quality of a reservoir. While the measurement of porosity is relatively easy, the measurement of the permeability of shale is complicated due to its viscoelastic behavior and organic-rich character. Conventional techniques such as steady state method (Figure 1) and pulse decay techniques (Figure 2) are time-consuming to measure extremely low permeability of shale. There are also numerous empirical formulas developed to approximate permeability based on porosity and pore sizes, etc. These empirical formulas have their limitations too such as failing to account for shale anisotropy and viscoelastic properties of shale; they are also proven to be inadequate for permeability estimation in the Nano-Darcy range (Comisky et al., 2007).

The bending of the beam under the three-point beam bending test is essentially a three-dimensional deformation of porous materials problem containing a viscous fluid. What makes the simulation of the test challenging is that shale possesses anisotropic and viscoelastic properties. To formulate the equations to solve the three-dimensional poroviscoelastic deformation of shale, the literatures on theory of deformations, anisotropic materials and poroviscoelasticity have been studied for this thesis.

The three-dimensional theory of deformation of porous materials saturated with a viscous fluid was developed by Biot (1941) and this is served as the fundamental governing equations of an isotropic elastic material. Later, the theory was extended to fit anisotropic elastic porous solids (Biot 1955). Not until 1956 did Biot introduce the

poroviscoelasticity theory where viscoelasticity is considered. More recently, Abousleiman et. Al. (1993) were able to isolate and quantify the simultaneous existence of poro- and viscoelastic effects. Numerical and analytical applications were subsequently developed in problems of boreholes (Abousleiman et al, 1996), anelastic strain recovery (Abousleiman et al, 1999 & Abousleiman et al, 2000), Articular Cartilage (Hoang and Abousleiman, 2009), human brain tissues (Mehrabian and Abousleiman, 2011) and shale reservoirs (Hoang and Abousleiman, 2012).

To solve the difficulty of measuring extremely low permeability and account for the viscoelastic properties, a new technique called three-point beam bending test was initially developed by Scherer in 1992 and recently used on shale. The experiment set up is illustrated below (Figure 3). Under the load, the fluid saturated porous beam is deformed and a pore pressure gradient is induced due to different strain in the skeleton. Fluid will start to flow out of the beam in the upper part and flow in in the lower part to achieve pressure equilibrium. The load required to sustain a constant deflection decreases as time elapses and is a function of permeability. The free body diagram is illustrated in Figure 4. Analytical solutions of the load decay under constant deflection have been obtained hence by recording the load along with time under constantly deformed beam, one could predict the permeability of the material by matching the collected data with analytical solutions. This method was originally designed to approximate the permeability of gel and cement paste, which are assumed to be isotropic poroelastic material when saturated with fluid (Scherer, 1992, 1994, 2000). Scherer also extended the solutions to transversely isotropic poroelastic materials (Scherer, 2004; Scherer et al.,

2007, 2009). And in 2012, experiments were performed on shale and permeability of shale was approximated accounting its viscoelastic behaviors and anisotropic characters.

The motivation behind this work is that scholars have claimed recently that shale is orthotropic besides being transversely isotropic in most cases (Crook et al. 2002). Therefore, obtaining orthotropic poroviscoelastic solutions for the three-point beam bending test is important. Figure 5 shows the calcareous laminated woodford shale under microscope, revealing strong degree of anisotropy (Sierra et al 2010). Up till this point, the analytical solutions have not been derived for orthotropic shale with consideration of viscoelastic properties. This work presents the orthotropic solutions to fill in the blank in this research area. The orthotropic constitution equations relating stress, strain and pore pressure (Hoang and Abousleiman, 2012), are used to formulate and derive the analytical solutions for the three-point beam bending problem.

To account for the viscoelasticity of shale, poroviscoelastic solutions for the three-point beam bending test have been derived in this work based on the correspondence principle (Hoang and Abousleiman, 2012).

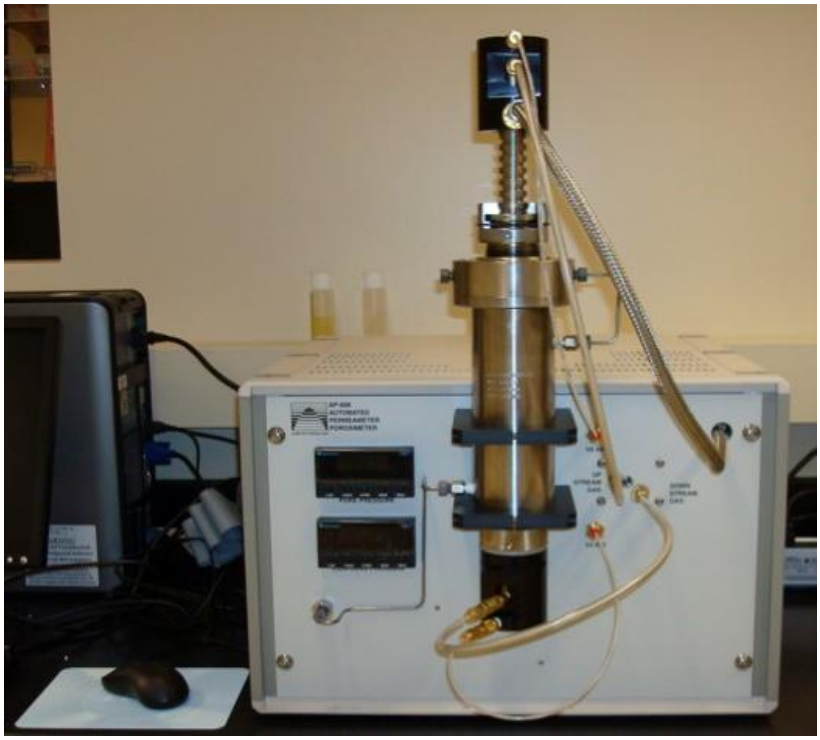


Figure 1. CoreTest AP608 instrument used to measure porosity and permeability: time consuming for shale (OU IC3 Lab)

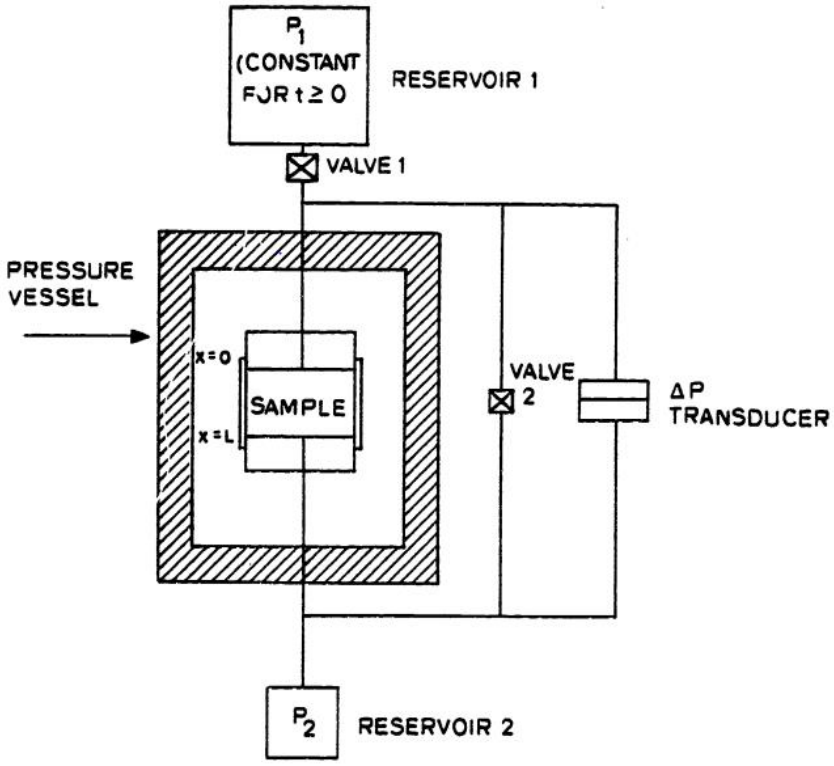


Figure 2. Pulse decay technique to measure rock permeability

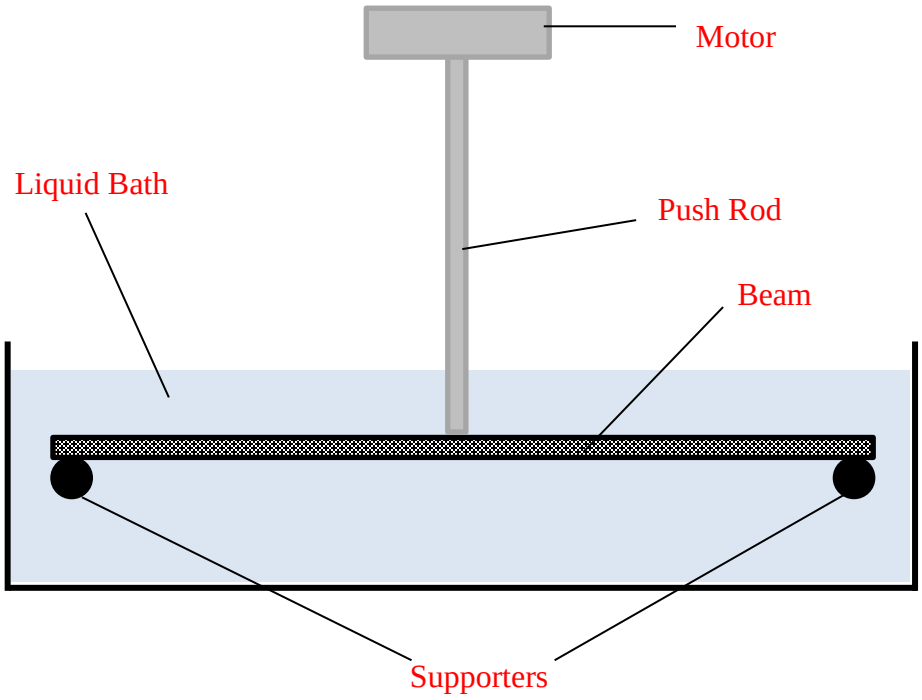


Figure 3. Schematic of three-point beam bending test: the beam is bent to a constant deflection in the center and immersed in the liquid bath.

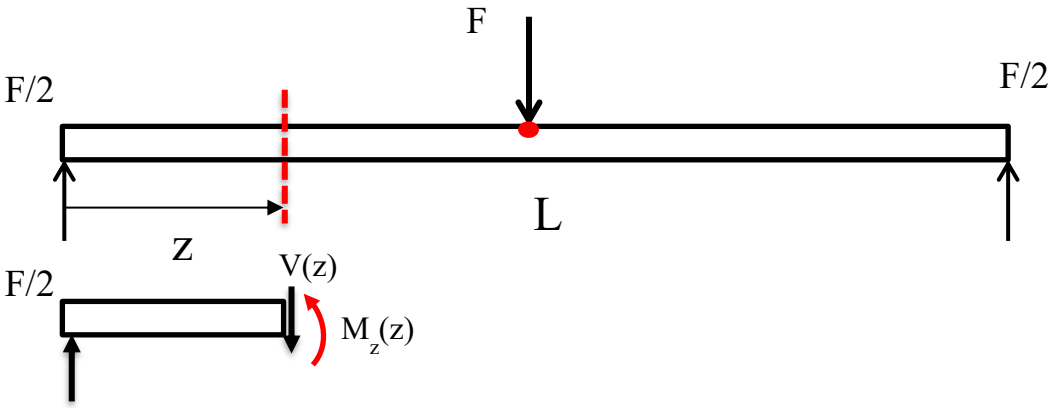


Figure 4. Free body diagram of the beam to which a force is applied in the three-point beam bending test

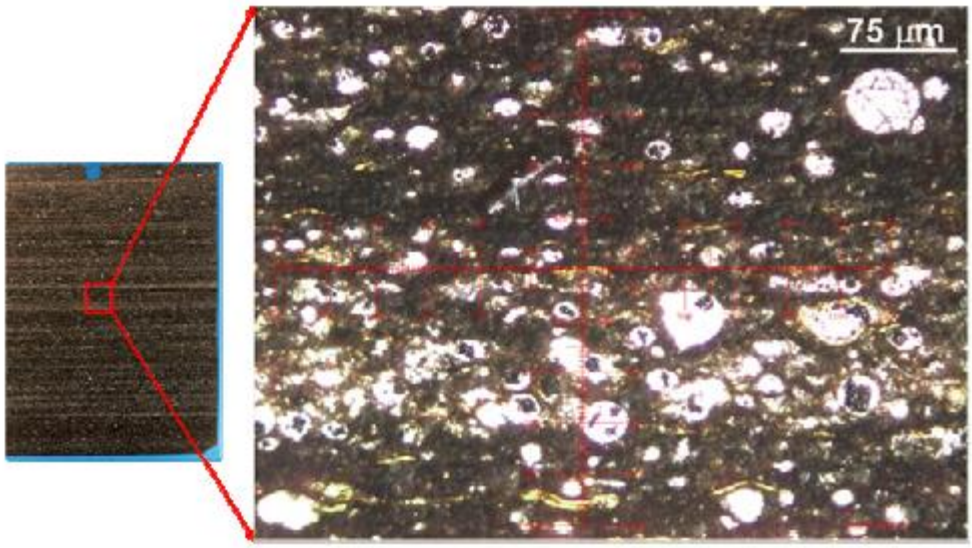


Figure 5. Thin section of the Woodford shale which reveals strong anisotropy (Sierra et al 2010).

Chapter 2: Problem Description

2.1 Laboratory Set-up

To measure the permeability using the three-point beam bending technique, the saturated sample is instantly bent to a certain degree and remained that constant deflection while the load required to sustain it is recorded. The equipment is shown in Figure 6 below. The beam is fully saturated before the test starts. Strictly careful procedures are conducted in order to prevent any air bubbles to intrude the medium (Scherer 2012). The samples are also laterally sealed to prevent any flow except in the direction of load. This is done intentionally so that permeability in only one direction is measured otherwise flow in more than one direction obscures the interpretation of the experiment (Scherer 2012).

Under constant deflection bending test, a load is exerted on the beam to sustain the constant deflection of the beam being placed on two supporters. The beam is kept in a liquid bath that contains the same liquid as the one saturated inside the beam.

In the experiment, the samples are sealed laterally on sides to prevent fluid flow. Fluid can only flow through the upper and lower surfaces of the beam and permeability is measured in the direction fluid can flow. Therefore, to approximate the permeability of an anisotropic shale which varies in different directions, the sample should be cored and placed in multiple ways. Take a transversely isotropic shale beam (figure 7) as an example

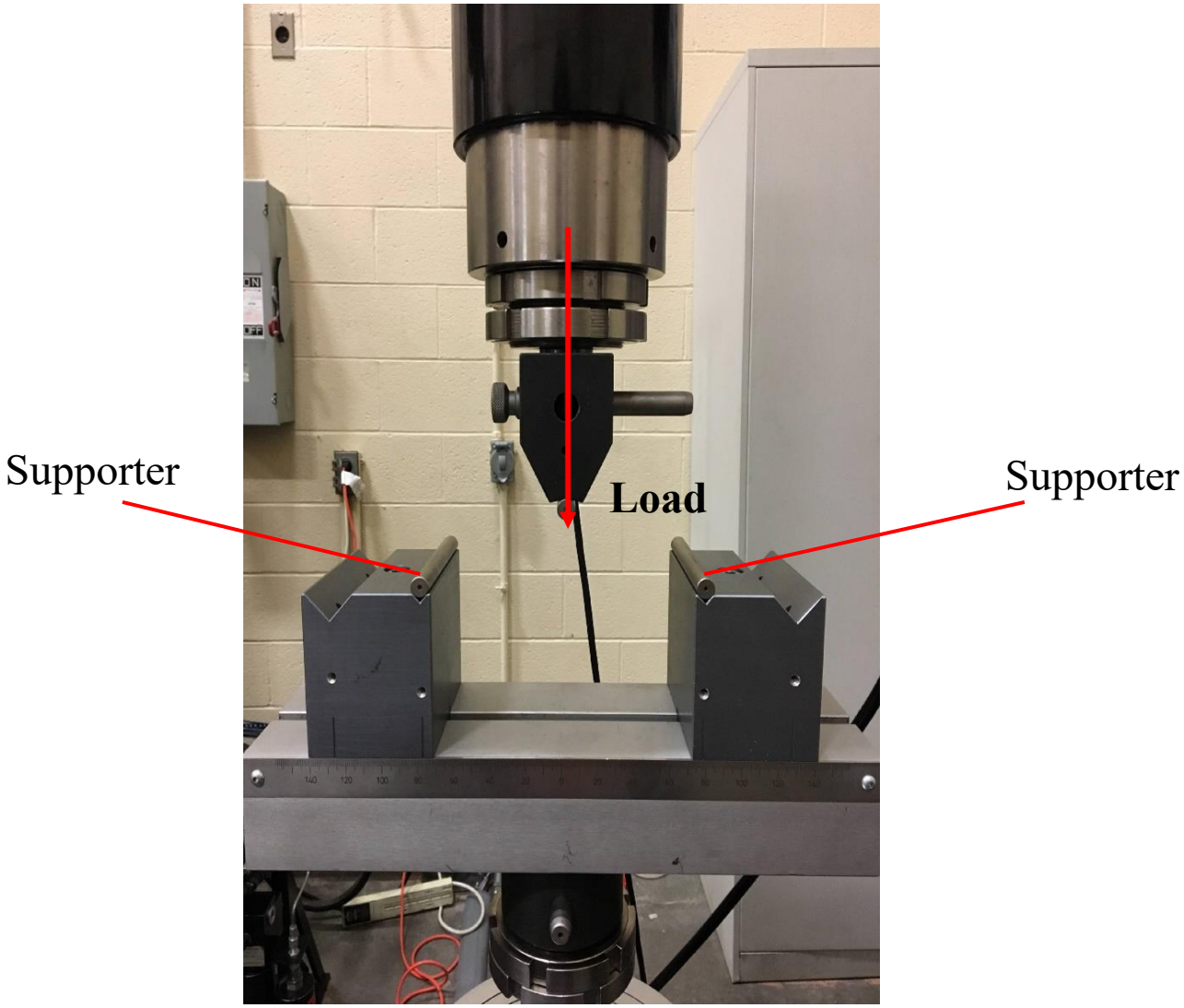


Figure 6. Three-point beam bending test equipment (OU PoroMechanics Lab)

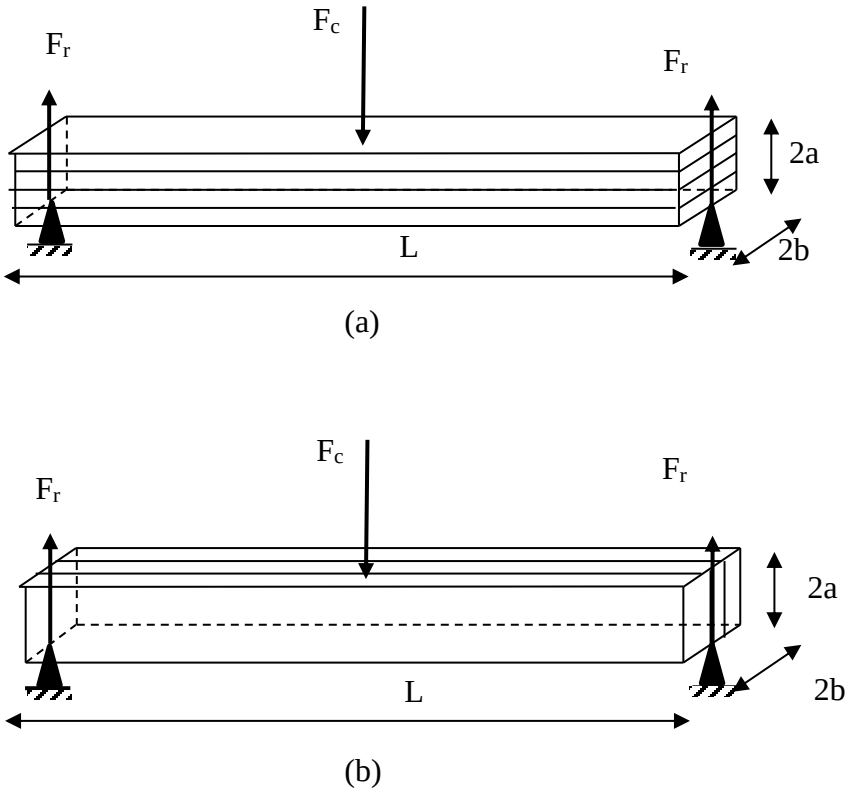


Figure 7. Placement of transversely isotropic beam: (a) measurement of permeability perpendicular to layers; (b) measurement of permeability parallel to layers

2.2 Simulation

The Cartesian coordinate system (Figure 8) is established in a way that x-axis is vertical, y-axis is lateral and the z-axis is longitudinal. The origin is in the center of the far-left surface of the beam.

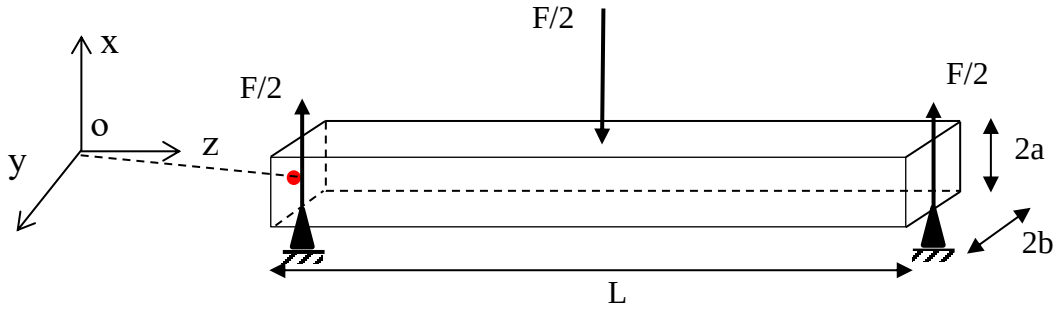
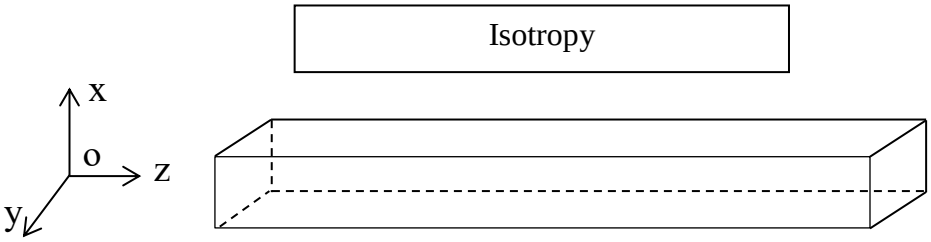


Figure 8. Cartesian coordinate for the three-point beam bending test throughout this work. The origin is in the center of the left most surface of the beam.

the lateral edges are sealed and fluid is only allowed to flow in the x direction. The simulation of the test is therefore treated as a one dimensional poroviscoelastic problem. In chapter 5, the solutions for pore pressure and load decay are presented under two-dimensional condition as fluid can flow in both x and y directions to fully study the experiment. Also, poroelastic solutions are derived and presented first before moving onto the more advanced poroviscoelastic solutions.

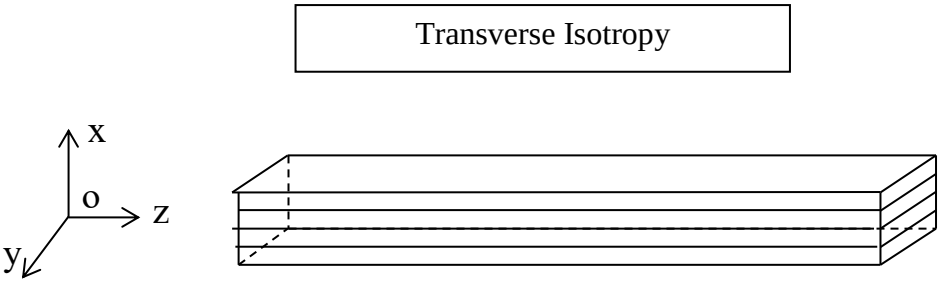
The author simulates the test and obtain the solutions for pore pressure and load decay by treating the beam as isotropic and anisotropic materials as illustrated below:

a



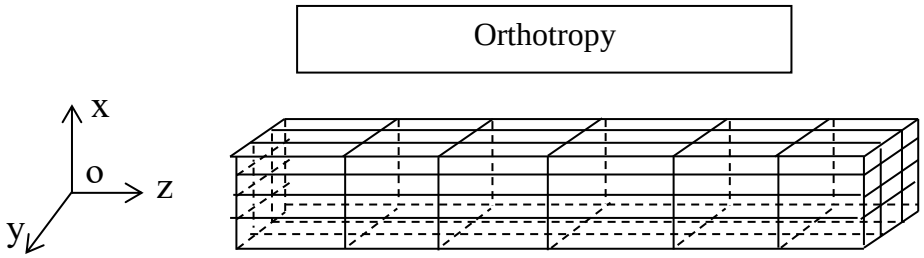
Young's Moduli	**Permeability**	**Poisson's Ratio**
$\mathbf{E_x=E_y=E_z}$	$\mathbf{k_x=k_y=k_z}$	$\mathbf{\upsilon_{xy}=\upsilon_{xz}=\upsilon_{yz}}$

b



Young's Moduli	Permeability	Poisson's Ratio
E_x, $E_y = E_z$	k_x, $k_y = k_z$	υ_{yx}, υ_{yz}

c



Young's Moduli	Permeability	Poisson's Ratio
E_x, E_y, E_z	k_x, k_y, k_z	υ_{xy}, υ_{xz}, υ_{yz}

Figure 9. (a) Isotropic, (b) transversely isotropic, and (c) orthotropic materials encountered in this work and how their properties distinguish from each other.

The beams are assumed to be homogeneous in the simulation, which means that the properties of the material are uniform throughout the beam at all locations.

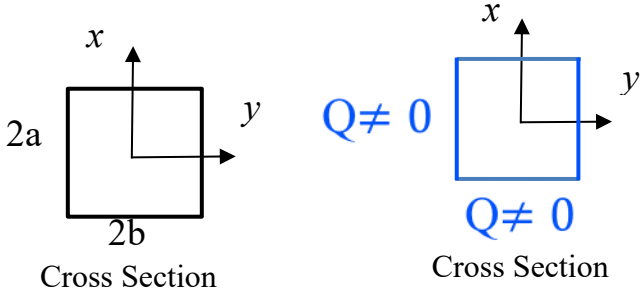
- Isotropic: Share the same physical properties in all direction

- Transverse Isotropic: Share the same physical properties in the isotropic plane but different physical properties in the direction perpendicular to the isotropic plane
- Orthotropic: no common physical properties in all direction

2.3 Initial and Boundary Conditions

Boundary conditions and initial conditions (detailed derivation in appendix) for the pore pressure in the simulate are illustrated below:

Table 1. Initial and Boundary conditions in the simulation

<table>
<tr><td>I.C.</td><td>$t = 0^+$</td><td>$p_0 = C_1 zx$
$C_1(M_{ij}, M, L, \Delta)$</td></tr>
<tr><td rowspan="3">B.C.</td><td colspan="2">

Cross Section Cross Section</td></tr>
<tr><td>$x = \pm a$</td><td>$p = 0$</td></tr>
<tr><td>$y = \pm b$</td><td>$p = 0$</td></tr>
</table>

Throughout the test, the beam is bent to a certain deflection and kept constant while the load required to sustain the constant deflection is recorded as the fluid is flowing through the surface the beam. Figure 10 is a schematic of the boundary conditions while reactions of the beam in the test.

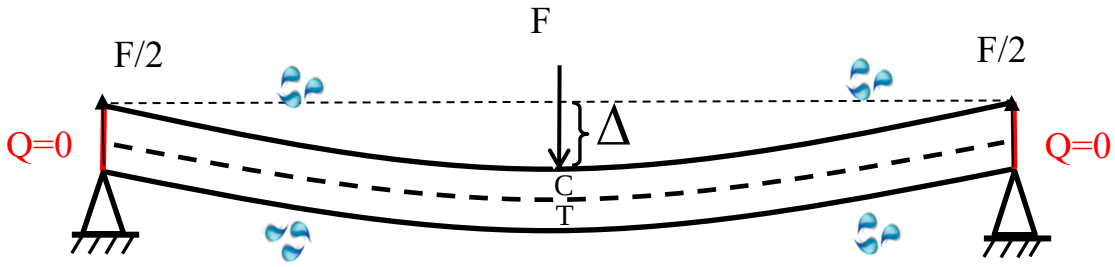


Figure 10. Boundary conditions in the simulation: beam is sealed laterally at two far ends. Fluid can flow in only x and y direction. C stands for compression, T stands for tension. Δ is the deflection.

Under constant deflection Δ, the beam experiences compression in the upper half and tension in the lower half (Figure 10) which is expressed as σ_z. There is no normal stress σ_x in x or σ_y in the y direction. At time t=0 when the deflection is instantly introduced, the variation of the fluid content $\zeta_0 = 0$ (the subscript 0 represents the initial value at t=0 everywhere in this paper) since the beam is incompressible initially and no fluid can instantly inside the medium. Therefore, the volumetric strain $\varepsilon_0 = 0$ as well since no fluid is drained.

Under constant deflection, the normal strain in z direction ε_z is a constant and expressed as:

$$\varepsilon_z = \frac{24\Delta xz}{L^3}, 0 \le z \le L/2$$
$$\varepsilon_z = \frac{24\Delta x(L-z)}{L^3}, L/2 \le z \le L \tag{2.1}$$

The bending moment M_z is related to the principal stress in z direction σ_z:

$$M_z = -\int_A \sigma_z x dA \tag{2.2}$$

Where A is the cross-sectional area of the beam. The load the related to the moment as:

$$F = \frac{2M_z}{z}, 0 \le z \le L/2$$
$$F = \frac{2M_z}{L-z}, L/2 \le z \le L \tag{2.3}$$

Before the test starts, the beam is fully saturated with the experimental fluid. Essentially during the test, the fluid inside the beam is squeezed out when a load is applied in the center of the beam to keep it bending at a constant deflection. During this process, the force needed to sustain the constant deflection decreases due to hydrodynamic relaxation and viscoelastic relaxation.

Chapter 3: Governing Equations

Throughout this work, the compressive stress and strain are taken as positive.

3.1 Orthotropic Poroelasticity

The stress, strain and pore pressure are related in the constitutive equations for orthotropic material as below (Abousleiman 2014):

$$\begin{pmatrix} \sigma_{xx} \\ \sigma_{yy} \\ \sigma_{zz} \end{pmatrix} = \begin{pmatrix} M_{11} & M_{12} & M_{13} \\ M_{12} & M_{22} & M_{23} \\ M_{13} & M_{23} & M_{33} \end{pmatrix} \begin{pmatrix} \varepsilon_{xx} \\ \varepsilon_{yy} \\ \varepsilon_{zz} \end{pmatrix} + \begin{pmatrix} \alpha_1 \\ \alpha_1 \\ \alpha_3 \end{pmatrix} p \tag{3.1}$$

$$p = M(\alpha_1 \varepsilon_{xx} + \alpha_2 \varepsilon_{yy} + \alpha_3 \varepsilon_{zz} + \zeta) \tag{3.2}$$

Where M_{ij} is the stiffness coefficients, α_i is the Biot's effective stress coefficient in the ith direction; p is the pore pressure, ζ is the variation of fluid content, M is the Biot's modulus, K_s is the grain bulk modulus, K_f is the fluid bulk modulus and ϕ is the porosity.

$$\begin{bmatrix} M_{11} & M_{12} & M_{13} \\ M_{12} & M_{22} & M_{23} \\ M_{13} & M_{23} & M_{33} \end{bmatrix}^{-1} = \begin{bmatrix} \frac{1}{E_x} & -\frac{\nu_{yx}}{E_y} & -\frac{\nu_{zx}}{E_z} \\ -\frac{\nu_{yx}}{E_y} & \frac{1}{E_y} & -\frac{\nu_{zy}}{E_z} \\ -\frac{\nu_{zx}}{E_z} & -\frac{\nu_{zy}}{E_z} & \frac{1}{E_z} \end{bmatrix}$$

$$\zeta = \frac{\Delta V_f}{V_{ref}}$$

$$\alpha_1 = 1 - \frac{M_{11} + M_{12} + M_{13}}{3K_s}$$

$$\alpha_2 = 1 - \frac{M_{12} + M_{22} + M_{23}}{3K_s} \tag{3.3}$$

$$\alpha_3 = 1 - \frac{M_{13} + M_{23} + M_{33}}{3K_s}$$

$$M = \frac{K_s}{(1 - M_{iijj}/9K_s) - \phi(1 - K_s/K_f)}$$

$$M_{iijj} = M_{11} + 2M_{12} + 2M_{13} + M_{22} + 2M_{23} + M_{33}$$

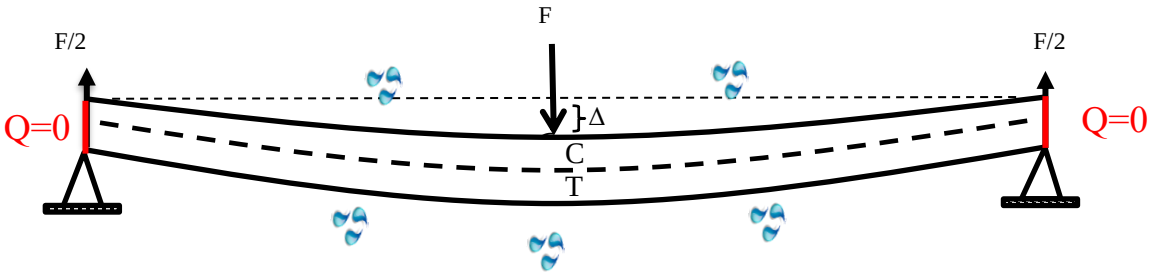


Figure 11. Schematic illustration of the bending of the beam under constant deflection when saturated with fluid. Fluid is squeezed out from the outer surface of the beam.

Only normal stress σ_{zz} in z direction exists in this bending test and both σ_{xx} and σ_{yy} are absent. When the beam is sustained at constant deflection, the longitudinal strain in z direction can be expressed as:

$$\varepsilon_{zz} = -24\frac{\Delta x z}{L^3}(0 \le z \le L/2)$$

$$\varepsilon_{zz} = -24\frac{\Delta x(L - z)}{L^3}(L/2 \le z \le L) \tag{3.4}$$

Above are the general governing equations for orthotropic materials. These equations can be used for isotropic and transversely isotropic materials as well by simply manipulating Young's Moduli E_1, E_2 and E_3. For instance, isotropic materials inherit uniform Young's moduli in all direction: $E_1 = E_2 = E_3$. Therefore, stiffness coefficients would equate each other as: (assuming $\nu_{21} = \nu_{31} = \nu_{32}$):

$$\begin{aligned} M_{11} &= M_{22} = M_{33} \\ M_{12} &= M_{13} = M_{23} \end{aligned} \tag{3.5}$$

Hence stiffness coefficient matrix would be simplified as:

$$\begin{bmatrix} M_{11} & M_{12} & M_{12} \\ M_{12} & M_{11} & M_{12} \\ M_{12} & M_{12} & M_{11} \end{bmatrix} \tag{3.6}$$

And therefore, other poroelastic parameters become:

$$\begin{aligned} \alpha_1 &= \alpha_2 = \alpha_3 \\ M_{iijj} &= 3M_{11} + 6M_{12} \end{aligned} \tag{3.7}$$

Governing equations of transversely isotropic materials are readily obtained in the same fashion by manipulating Young's Moduli.

Other governing equations include Darcy's Law and continuity equations as listed below:

- Darcy's Law:

$$\begin{aligned} q_x &= \frac{k_x}{\mu}\frac{\partial p}{\partial x} \\ q_y &= \frac{k_y}{\mu}\frac{\partial p}{\partial y} \end{aligned} \tag{3.8}$$

Where q_x and q_y are the fluxes along x and y direction, k_x and k_y are the permeability along x and y direction and μ denotes the fluid viscosity. Assumption has made it that

there is no flow in the z direction because the length is much longer than the vertical and lateral dimension so that all of the low will perpendicular to z axis (Scherer, 1992).

- Continuity equation:

$$\frac{\partial \zeta}{\partial t} = -\frac{\partial q_x}{\partial x} - \frac{\partial q_y}{\partial y} \tag{3.9}$$

Which indicates that the rate of fluid content variation is equal in magnitude and opposite in direction compared to fluid flow rate.

3.2 Orthotropic Poroviscoelasticity

Compared to poroelasticity, Poroviscoelasticity captures the visco properties of the materials: Young's Moduli are now time dependent. Most of the shales are viscoelastic materials, therefore a poroviscoelastic model would be more accurate than a poroelastic one.

To simulate the viscoelasticity of the beam, a model that transforms Young's Moduli to be time-dependent is needed. Two models are used in this study to present an insight on how viscoelastic beams are handled differently than elastic ones in the simulation.

Zener Model:

$$E(t) = E_0[1 - \alpha + \alpha e^{-\frac{t}{\tau}}] \tag{3.10}$$

Sone-Zoback Model:

$$E(t) = E_0 t^{-\beta} \tag{3.11}$$

With the aid of correspondence principle (Hoang and Abousleiman, 2012), which states that

"Any constituitive relation or formula for material coefficients of anisotropic linear poroviscoelasticity can be obtained from the corresponding expression in

anisotropic linear poroelasticity by replacing multiplication with Stieltjes convolution product." Therefore Eq. 4.1 and 4.2 become:

$$\begin{pmatrix}\sigma_{xx}\\ \sigma_{yy}\\ \sigma_{zz}\end{pmatrix}=\begin{pmatrix}M_{11}(t) & M_{12}(t) & M_{13}(t)\\ M_{12}(t) & M_{22}(t) & M_{23}(t)\\ M_{13}(t) & M_{23}(t) & M_{33}(t)\end{pmatrix}\otimes\begin{pmatrix}\varepsilon_{xx}\\ \varepsilon_{yy}\\ \varepsilon_{zz}\end{pmatrix}+\begin{pmatrix}\alpha_1\\ \alpha_1\\ \alpha_3\end{pmatrix}\otimes p \tag{3.12}$$

$$p=M(t)\otimes(\alpha_1(t)\otimes\varepsilon_{xx}+\alpha_2(t)\otimes\varepsilon_{yy}+\alpha_3(t)\otimes\varepsilon_{zz}+\zeta) \tag{3.13}$$

Where $\otimes$ denotes the Stieltjes integral:

$$f(t)\otimes g(t)=\int_{-\infty}^{t} f(t-\tau)dg(\tau) \tag{3.14}$$

The correspondence principle also states that "the formulation and solution to the same boundary and initial value problem in anisotropic linear porovscoelasticity can be obtained from those in poroelasticity by replacing poroelastic material coefficients with The Carson transform of the poroviscoelastic counterparts." Therefore by applying Laplace and Carson transform to Eqs. 4.12 and 4.13 yields:

$$\begin{pmatrix}\tilde{\bar{\sigma}}_{xx}\\ \tilde{\bar{\sigma}}_{yy}\\ \tilde{\bar{\sigma}}_{zz}\end{pmatrix}=\begin{pmatrix}\bar{M}_{11} & \bar{M}_{12} & \bar{M}_{13}\\ \bar{M}_{12} & \bar{M}_{11} & \bar{M}_{13}\\ \bar{M}_{13} & \bar{M}_{13} & \bar{M}_{33}\end{pmatrix}\begin{pmatrix}\tilde{\bar{\varepsilon}}_{xx}\\ \tilde{\bar{\varepsilon}}_{yy}\\ \tilde{\bar{\varepsilon}}_{zz}\end{pmatrix}+\begin{pmatrix}\bar{\alpha}_1\\ \bar{\alpha}_1\\ \bar{\alpha}_3\end{pmatrix}\tilde{\bar{p}} \tag{3.15}$$

$$\tilde{\bar{p}}=\bar{M}(\bar{\alpha}_1\tilde{\bar{\varepsilon}}_{xx}+\bar{\alpha}_1\tilde{\bar{\varepsilon}}_{yy}+\bar{\alpha}_3\tilde{\bar{\varepsilon}}_{zz}+\tilde{\bar{\zeta}}) \tag{3.16}$$

With (~) denoting the Laplace Transform and (¯) denoting Carson Transform.

Laplace transform: $F(s)=\int_0^{\infty} f(t)e^{-st}dt$ (4.17)

Carson Transform: $F(s)=s\int_0^{\infty} f(t)e^{-st}dt$ (4.18)

The anisotropic poroviscoelastic parameters are expressed in the new form of:

$$
\begin{aligned}
\overline{\alpha}_1 &= 1 - \frac{\overline{M}_{11} + \overline{M}_{12} + \overline{M}_{13}}{3K_s} \\
\overline{\alpha}_2 &= 1 - \frac{\overline{M}_{12} + \overline{M}_{22} + \overline{M}_{23}}{3K_s} \\
\overline{\alpha}_3 &= 1 - \frac{\overline{M}_{13} + \overline{M}_{23} + \overline{M}_{33}}{3K_s} \\
\overline{M} &= \frac{K_s}{(1 - \overline{M}_{iijj} / 9K_s) - \phi(1 - K_s / K_f)} \\
\overline{M}_{iijj} &= \overline{M}_{11} + 2\overline{M}_{12} + 2\overline{M}_{13} + \overline{M}_{22} + 2\overline{M}_{23} + \overline{M}_{33}
\end{aligned}
\tag{3.17}
$$

This theory grants solutions to poroviscoelasticity readily as long as the solutions to poroelasticity are available and they share the same boundary and initial conditions.

Chapter 4: Analytical Solutions

The beam is sustained under constant deflection throughout the test. Under constant deflection condition, the analytical solutions of the load will decrease with time for all three cases. However, the rate of load relaxation is different depending on whether it is hydrodynamic relaxation, viscoelastic relaxation or the combination of the two and the boundary conditions: sealed in one direction or sealed in two directions.

Analytical solutions for pore pressure and work for each case are presented below:

4.1 Poroelastic Solutions

By combining Darcy's Law and continuity equations Eqs. 4.8, 4.9, the following equation is obtained:

$$\frac{\partial \zeta}{\partial t} = -\frac{k_x}{\mu}\frac{\partial^2 p}{\partial x^2} - \frac{k_y}{\mu}\frac{\partial^2 p}{\partial y^2} \tag{4.1}$$

This is the volume balance equation: the left-hand side represents the volume change of the system and the right-hand side is the sum of the fluid going in and out of the system. ζ can be expressed as a function of pore pressure p and longitudinal strain ε_{zz} from Eqs. 4.1, 4.2 as:

$$\zeta = \left(\frac{1}{M} - \frac{\alpha_1(\alpha_1 M_{22} - \alpha_2 M_{12}) - \alpha_2(\alpha_1 M_{12} - \alpha_2 M_{11})}{M_{12}M_{12} - M_{11}M_{22}}\right)p - \left(\frac{\alpha_1(M_{13}M_{22} - M_{23}M_{12}) - \alpha_2(M_{13}M_{12} - M_{23}M_{11})}{M_{12}M_{12} - M_{11}M_{22}} + \alpha_3\right)\varepsilon_{zz} \tag{4.2}$$

Therefore, the left-hand side of Eq. 5.1 becomes:

$$\left(\frac{1}{M} - \frac{\alpha_1(\alpha_1 M_{22} - \alpha_2 M_{12}) - \alpha_2(\alpha_1 M_{12} - \alpha_2 M_{11})}{M_{12}M_{12} - M_{11}M_{22}}\right)\frac{\partial p}{\partial t} - \left(\frac{\alpha_1(M_{13}M_{22} - M_{23}M_{12}) - \alpha_2(M_{13}M_{12} - M_{23}M_{11})}{M_{12}M_{12} - M_{11}M_{22}} + \alpha_3\right)\frac{\partial \varepsilon_{zz}}{\partial t} \tag{4.3}$$

Eq. 4.4 indicates that ε_{zz} is time-independent, thus $\frac{\partial \varepsilon_{zz}}{\partial t} = 0$ and Eq. 5.3 becomes

$$(\frac{1}{M}-\frac{\alpha_1(\alpha_1 M_{22}-\alpha_2 M_{12})-\alpha_2(\alpha_1 M_{12}-\alpha_2 M_{11})}{M_{12}M_{12}-M_{11}M_{22}})\frac{\partial p}{\partial t}=\frac{k_x}{\mu}\frac{\partial^2 p}{\partial x^2}+\frac{k_y}{\mu}\frac{\partial^2 p}{\partial y^2} \tag{4.4}$$

After normalizing t, x and y and manipulating Eq. 5.4, it can be transformed into:

$$\frac{\partial p}{\partial \theta}=\frac{\partial^2 p}{\partial v^2}+\kappa\frac{\partial^2 p}{\partial w^2} \tag{4.5}$$

Where $\theta = t/\tau$ with $\tau = \dfrac{(\frac{1}{M}-\frac{\alpha_1(\alpha_1 M_{22}-\alpha_2 M_{12})-\alpha_2(\alpha_1 M_{12}-\alpha_2 M_{11})}{M_{12}M_{12}-M_{11}M_{22}})\mu a^2}{k_x}$, $v = x/a$

and $w = y/b$. 2a and 2b are the depth and width of the beam and $\kappa = \dfrac{a^2 k_y}{b^2 k_x}$.

Pore pressure is therefore a function a time t and location x and y inside the beam and is expressed as $p(v, w, \theta)$.

Take boundary condition 1 as the boundary condition for the Eq. 5.5:

$$p(\pm 1, w, \theta) = p(v, \pm 1, \theta) = 0 \tag{4.6}$$

The boundary conditions indicate that at outer surface of the beam the pore pressure is 0 psi.

The initial condition for the Eq. 5.5 is obtained from Eq. 5.2 by setting $\zeta = 0$ because at $t = 0^+$ no fluid variation has happened yet. Therefore, the initial condition is

$$p(v, w, 0) = 24\frac{\frac{\alpha_1(M_{13}M_{22}-M_{23}M_{12})}{M_{12}M_{12}-M_{11}M_{22}}-\frac{\alpha_2(M_{13}M_{12}-M_{23}M_{11})}{M_{12}M_{12}-M_{11}M_{22}}+\alpha_3}{\frac{1}{M}-\frac{\alpha_1(\alpha_1 M_{22}-\alpha_2 M_{12})}{M_{12}M_{12}-M_{11}M_{22}}+\frac{\alpha_2(\alpha_1 M_{12}-\alpha_2 M_{11})}{M_{12}M_{12}-M_{11}M_{22}}}\frac{\Delta a}{L^3}zv \tag{4.7}$$

With the Eqs. 5.5, 5.6 and 5.7, a complete PDE with boundary and initial conditions are solved (detailed explanation is in Appendix) and the solution to the pore pressure p is below:

Pore pressure: $p = 4p_0 \sum_{m=1}^{\infty}\sum_{n=1}^{\infty} \frac{(-1)^m}{a_m}\frac{(-1)^n}{b_n}\sin(a_m v)\cos(b_n w)e^{-(\kappa b_n^2 + a_m^2)\theta}$ (4.8)

The three-point bending beam test only creates uniaxial stress along the z-axis therefore $\sigma_{xx} = \sigma_{yy} = 0$. Manipulating Eq. 4.1 (Detailed explanation is in Appendix), the uniaxial stress along z-axis can be expressed as:

$$\sigma_{zz} = [\frac{M_{13}(M_{13}M_{22} - M_{23}M_{12}) - M_{23}(M_{13}M_{12} - M_{23}M_{11})}{M_{12}M_{12} - M_{11}M_{22}} + M_{33}]\varepsilon_{zz} + [\frac{M_{13}(\alpha_1 M_{22} - \alpha_2 M_{12}) - M_{23}(\alpha_1 M_{12} - \alpha_2 M_{11})}{M_{12}M_{12} - M_{11}M_{22}} + \alpha_3]p \quad (4.9)$$

Where $\varepsilon_{zz} = -24\frac{\Delta x z}{L^3}(0 \le z \le L/2)$ or $\varepsilon_{zz} = -24\frac{\Delta x(L-z)}{L^3}(L/2 \le z \le L)$ per Eq. 4.4

Moment at the cross section of the beam is expressed as

$$M_z = \int_A \sigma_{zz} x dA \quad (4.10)$$

Where $dA = dxdy$

Therefore, after integration, the bending moment M_z could be obtained. The equilibrium equation for the beam under small deflection:

$$\begin{aligned} M_z &= \frac{z}{2}F_C(0 \le z \le L/2) \\ M_z &= \frac{(L-z)}{2}F_C(L/2 \le z \le L) \end{aligned} \quad (4.11)$$

where F_C is the load required to sustain the constant deflection and could be obtained as long as M_z is solved (detailed explanation is in Appendix C).

$$\begin{aligned} F_C &= \frac{2M_z}{z}(0 \le z \le L/2) \\ F_C &= \frac{2M_z}{L-z}(L/2 \le z \le L) \end{aligned} \quad (4.12)$$

4.2 Poroviscoelastic Solutions

When the beam is viscoelastic in the simulation, which means that the Young's Moduli are time-dependent, the three-point beam bending test simulation becomes a poroviscoelastic problem. With the aid of correspondence principle (introduced in chapter 4), the solutions are easily obtained from poroelastic solutions. Since poroviscoelastic simulation shares the same boundary and initial conditions as the ones for poroelastic simulation, the solutions are in the same form but in Laplace domain:

Pore pressure: $$\tilde{\bar{p}} = 4\bar{p}_0 \sum_{m=1}^{\infty}\sum_{n=1}^{\infty} \frac{(-1)^m}{a_m}\frac{(-1)^n}{b_n}\sin(a_m v)\cos(b_n w)\tilde{e}^{-(\bar{\kappa}b_n^2+a_m^2)\bar{\theta}} \tag{4.13}$$

Load:

$$\begin{aligned} \tilde{\bar{F}}_C &= \frac{2\tilde{\bar{M}}_z(z)}{z}(0 \le z \le L/2) \\ \tilde{\bar{F}}_C &= \frac{2\tilde{\bar{M}}_z(z)}{L-z}(L/2 \le z \le L) \end{aligned} \tag{4.14}$$

With (~) denoting the Laplace Transform and ($\bar{}$) denoting Carson Transform.

To transform them back to time domain, Stehfest Method (Abousleiman, etc., 1994) is used.

For detailed derivation of above solutions, please refer to the appendix. With the analytical solutions on hand, the author was able to study the pore pressure change when different input was applied in order to study how sensitive pore pressure is to each parameter, such as Young's Modulus, permeability and so on. The analytical solution of the load is by all means the most important one. As long as the experiment data of load of the three point beam bending test under constant deflection is accessible, one is able to match the analytical solution to the data and approximate the permeability of the beam. The method of approximation of permeability will be addressed in the further chapter.

Chapter 5: Numerical Examples

In the petroleum engineering discipline, permeability of the source rock is an essential information to engineers since it provides insight on how easy the valuable fluid can flow to borehole. Therefore, knowing permeability will aid in determining drilling and production strategies and help in making important executive decisions. The three-point beam bending test is an alternative method of measuring permeability to conventional method. The alternative method takes much less time and gives accurate results. To fully study such a test, the author simulated the test using Mathematica and derive the analytical solutions for the pore pressure change inside the beam and the load decay under a constant deflection test.

To make the simulation as close to reality as possible, the beam is treated as viscoelastic, which means that the Young's Moduli are time-dependent. For elastic materials, one exerted stress corresponds to one strain according to Hooke's Law. However, a viscoelastic material exhibits both elastic deformation and viscous deformation (Huang & Ghassemi, 2013). The well-known spring-dashpot models are often used to utilized for viscoelastic behaviors: Spring is used to represent elastic component of the material and its constitutive equation is given as

$$\sigma = K\varepsilon$$

where K is the stiffness of the spring. Dashpot is used to represent the viscous component of the material and its constitutive equation is shown below as:

$$\sigma = \eta\dot{\varepsilon} = \eta\frac{d\varepsilon}{dt}$$

Where η is the dashpot viscosity (Hoang 2011).

Numerous linear viscoelastic models have been constructed with springs and dashpots organized in various pattern to simulate distinguished viscoelastic behaviors. Figure 12 presents the three typical models that are the commonly used.

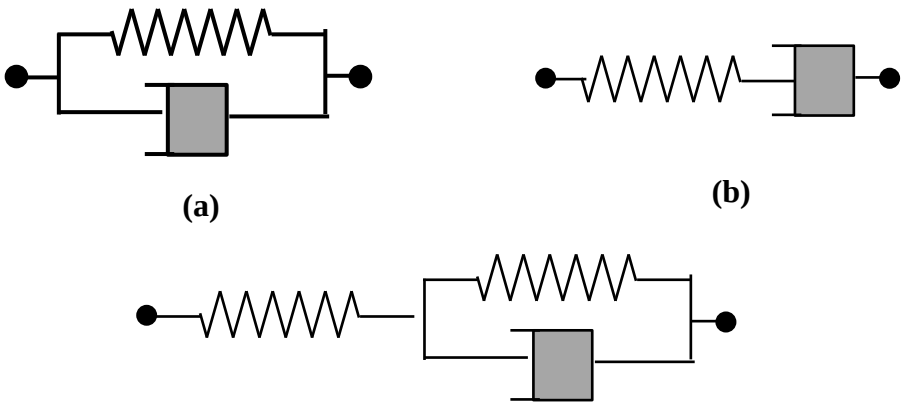


Figure 12. Schemetic representation of different viscoelastic models: (a) Kelvin model; (b) Maxwell model and (c) Zener model.

Zener and Sone-Zoback models are used in the simulation to demonstrate how viscoelastic materials behave differently than elastic materials. If the materials exhibit more complicated viscoelastic behaviors, more advanced models should be used.

The solution for elastic beam is also obtained to serve as a comparable counterpart. The following are the unchanging mechanical properties: Porosity $\phi = 15\%$, Poisson's Ratio $\nu = 0.3$ and grain bulk modulus $K_S = 40GPa$.

Two models are used in this study to simulate the viscoelastic properties of the beam:

Zener Model:

$$E(t) = E_0[1-\alpha+\alpha e^{-\frac{t}{\tau}}] \tag{5.1}$$

Where α is the percentage of the maximum Young's Modulus decay at infinitely long time to the initial value of it, and τ is the characteristic relaxation time.

The bigger the α is, the smaller value Young's Modulus can decay to.

The smaller τ the is, the faster the Young's Modulus decays.

Sone-Zoback Model:

$$E(t) = E_0 t^{-\beta} \tag{5.2}$$

Where β is characterizes the relaxation rate: higher β leads to a faster rate of decline in Young's Moduli and vice versa. However, Young's moduli in Sone-Zoback Model will not drop asymptotically at infinite time as young's moduli in Zener model does.

The beam is set to be 80 mm in length, 4 mm in width and depth as illustrated below. The constant deflection is maintained at 1mm at the center of the beam.

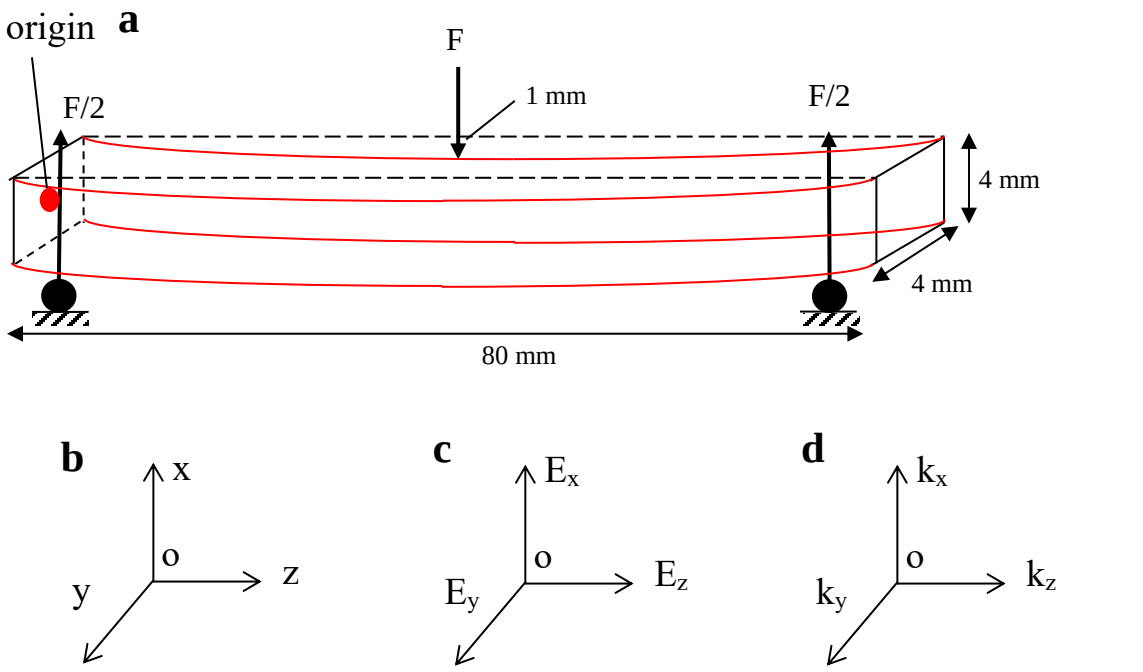
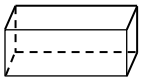
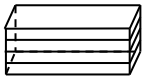
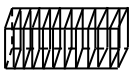
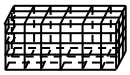


Figure 13. (a) The dimension and constant deflection of the beam in the three-point beam bending test simulation and (b) (c) (d) the definition of the mechanical properties in each direction: Young's Moduli and permeability in x, y and z direction are E_x, k_x, E_y, k_y, E_z and k_z respectively.

The above Cartesian coordinates are established for the entire work such that the beam is always placed in the way that x-axis is parallel to the depth of the beam, y-axis is parallel to the width of the beam and z-axis is parallel to the length of the beam. Therefore, to make the beam isotropic, transversely isotropic and orthotropic in the simulation, the author needs to adjust input (Young's Moduli and permeability) in each direction.

Table 2. Mechanical properties of isotropic, transversely isotropic and orthotropic beam used in the simulation of the three-point beam bending test

	Isotropic	Transversely Isotropic			Orthotropic
		Case 1	Case 2	Case 3	
					
Young's Moduli, E	$E_x = E_y = E_z = 5.6GPa$	$E_x = 4.6GPa$ $E_y = E_z = 5.6GPa$	$E_y = 4.6GPa$ $E_x = E_z = 5.6GPa$	$E_z = 4.6GPa$ $E_x = E_y = 5.6GPa$	$E_x = 4.6GPa$ $E_y = 2.6GPa$ $E_z = 5.6GPa$
Permeability, k	$k_x = k_y = k_z = 0.4nD$	$k_x = 0.2nD$ $k_y = k_z = 0.4nD$	$k_y = 0.2nD$ $k_x = k_z = 0.4nD$	$k_z = 0.2nD$ $k_x = k_y = 0.4nD$	$k_x = 0.2nD$ $k_y = 0.4nD$ $k_z = 0.4nD$

The properties of the fluid input into the simulation are: Viscosity, $\mu = 1cp$ and fluid bulk modulus, $K_f = 0.8GPa$

Two important outcomes are studied thoroughly: pore pressure change and load decay. The rest of this chapter will dedicate to listing plots of pore pressure change and

load decay under various conditions. For example, poroelastic solutions and poroviscoelastic solutions are compared to observe the influence of viscoelasticity; isotropic, transversely isotropic and orthotropic solutions are compared to detect the influence of anisotropy; Also two viscoelastic models are investigated.

5.1 Effects of Anisotropy

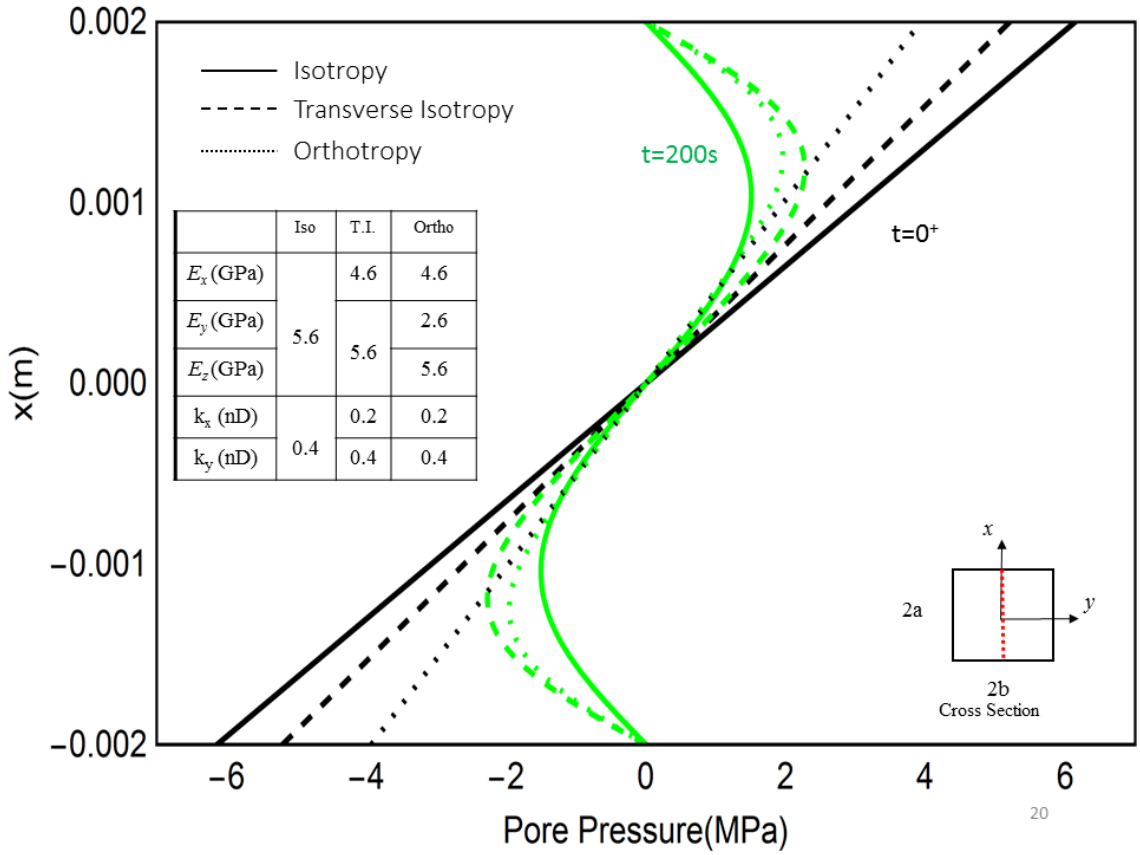
In this section, the beam is assigned different mechanical properties to simulate isotropic, transverly isotropic and orthotropic materials. Poroelastic solutions are

Isotropy: $E_x=E_{y=}E_z$ = 5.6 GPa; $k_x= k_y=k_z=0.4nD$.

Transversely Isotropy: E_x = 4.6 GPa, $E_y=E_z$= 5.6 GPa; k_x= 0.2nD, $k_y=k_z=0.4nD$.

Orthotropy: E_x= 4.6 GPa, E_y=2.6 GPa, E_z = 5.6 GPa; k_x= 0.2nD, $k_y=k_z=0.4nD$.

Figure 14 shows the pore pressure distribution along x-axis for isotropic, transversely isotropic and orthotropic beams. The mechanical properties that set these three cases different are permeability and Young's Moduli. The initial pore pressure jump at $t=0^+$ for isotropic beam is the highest among the three. This is a result of highest overall stiffness of the isotropic beam, followed by transversely isotropic beam and orthotropic beam at last. The initial pore pressure jump is dominated by Young's Moduli and is not influenced by the permeability. By looking at the pore pressure for each case t= 200s isotropic beam also exhibits the highest pore pressure drop rate, followed by transversely isotropic beam and orthotropic beam. This phenomenon could be explained by the highest overall hydrodynamic relaxation of the orthotropic beam: higher Young's Moduli and higher permeability boosts the hydrodynamic relaxation. Similar trends could be observed as well in Figure 15 showing the pore pressure distribution along y-axis.



	Iso	T.I.	Ortho
E_x (GPa)	5.6	4.6	4.6
E_y (GPa)		5.6	2.6
E_z (GPa)			5.6
k_x (nD)	0.4	0.2	0.2
k_y (nD)		0.4	0.4

Figure 14. Poroelastic pore pressure distribution along x-axis at y=0mm and z=40mm at variable times for isotropic, transversely isotropic and orthotropic beams.

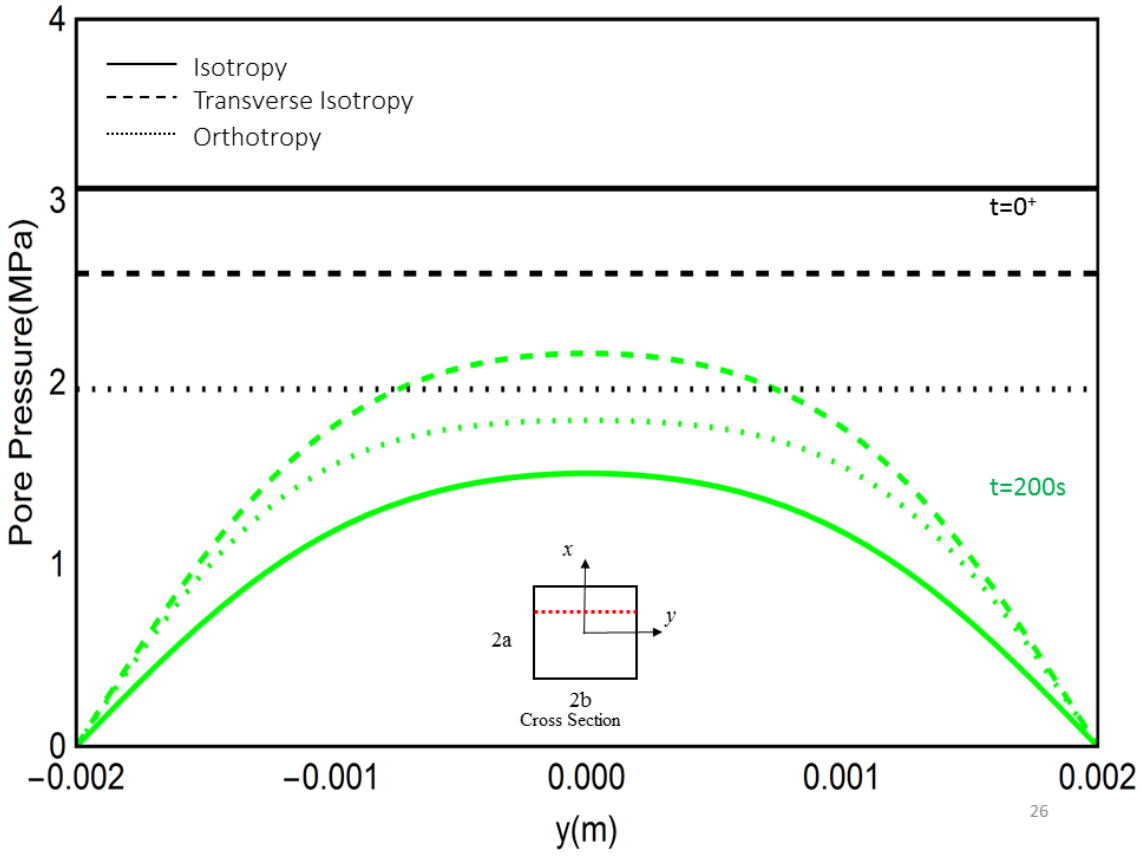


Figure 15. Poroelastic pore pressure distribution along y-axis at x=1mm and z=40mm at variable times for isotropic, transversely isotropic and orthotropic beams.

Figure 16 contains the load decay along with time for isotropic, transversely isotropic and orthotropic beams. Isotropic beam with the overall highest stiffness ends up with the highest initial load; it also exhibits the fastest load decay rate due to the highest hydrodynamic relaxation. The transversely isotropic beam has the second largest initial load and second fastest hydrodynamic relaxation rate. The orthotropic beam has the smallest initial load and the slowest hydrodynamic relaxation rate among the three. This result is intuitive and concurs with the comparison of the pore pressure changes.

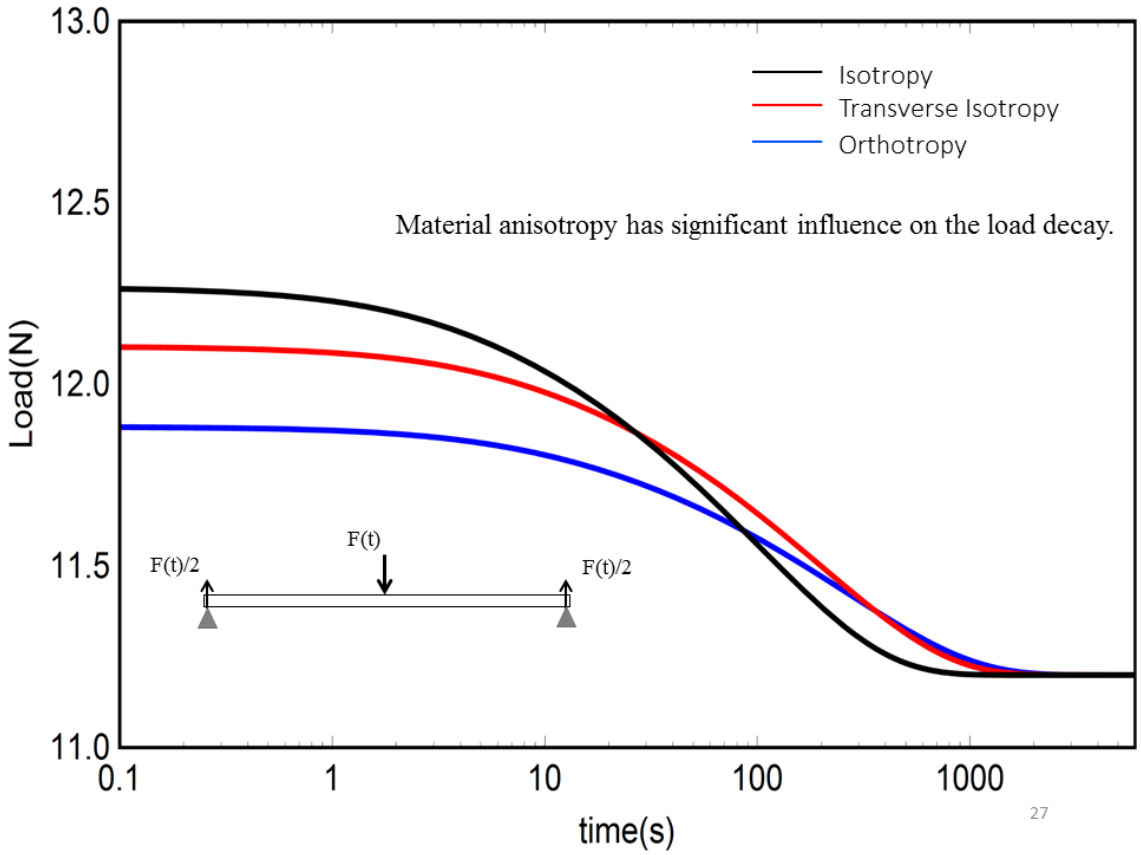


Figure 16. Poroelastic load decay to sustain a 1mm constant deflection for isotropic, transversely isotropic and orthotropic beams.

5.2 Effects of Viscoelastic Properties

In this section, the beam is simulated to be a orthotropic material with $E_x(0^+)$ = 4.6 GPa, $E_y(0^+)$=2.6 GPa, $E_z(0^+)$ = 5.6 GPa; k_x= 0.2nD, k_y=k_z=0.4nD. Zener Model is used to simulate the viscoelastic relaxation: $E(t) = E_0[1-\alpha+\alpha e^{-\frac{t}{\tau}}]$ with $\alpha = 0.5$ and $\tau = 1000s$.

Figure 17 represents the pore pressure distribution along the x-axis at y=0 mm and z=40 mm along with different times. The pore pressure is indicated as positive value when x > 0 mm and negative when x < 0mm. This sign change is caused by compression in the upper half of the beam and tension in the lower half of the beam. Initial pore

pressure jump at $t=0^+$s is in a linear relationship along the x-axis because no fluid has had flown out of the beam yet when the deflection is applied instantly. $t=0^+$s is also the only time when the pore pressure at the upper and lower boundary (x=2 mm and x=-2 mm) is not equal to zero. At any time after the constant deflection is instantly applied, the pore pressure at the boundary is 0 Psi since the boundary is permeable and exposed to atmosphere pressure. The pore pressure along x-axis decreases as time elapses. The is phenomenon is called hydrodynamic relaxation. Eventually the pore pressure will reach equilibrium where the pore pressure drops to 0. However, the rate of the pressure drop seems to decrease as well as time goes. The rate of pore pressure drop is directly related to the flow rate of the flow leaking out of the beam. According to Darcy's Law $q_x = -\frac{k_x}{\mu}\frac{\partial p}{\partial x}$, the flow rate in x direction is proportionally to pressure difference $\frac{\partial p}{\partial x}$. At $t=0^+$s, the pressure different is biggest; therefore, the flow rate is biggest, so is the pore pressure drop. As pressure drops, the flow rate decreases, hence leads to a slower pressure drop.

The pressure drop is also faster for poroviscoelastic case than that of the poroelastic case because poroviscoelastic material exhibits viscoelastic relaxation besides hydrodynamic relaxation under constant deflection. Young's Moduli decreases with time for poroviscoelastic material, therefore the load needed to sustain the constant deflection drops. Thus, the pore pressure induced in the pores also drops. Such effect is called viscoelastic relaxation, which contributes to the pore pressure drop. One can notice that,

compared to hydrodynamic relaxation, viscoelastic relaxation is much less significant.

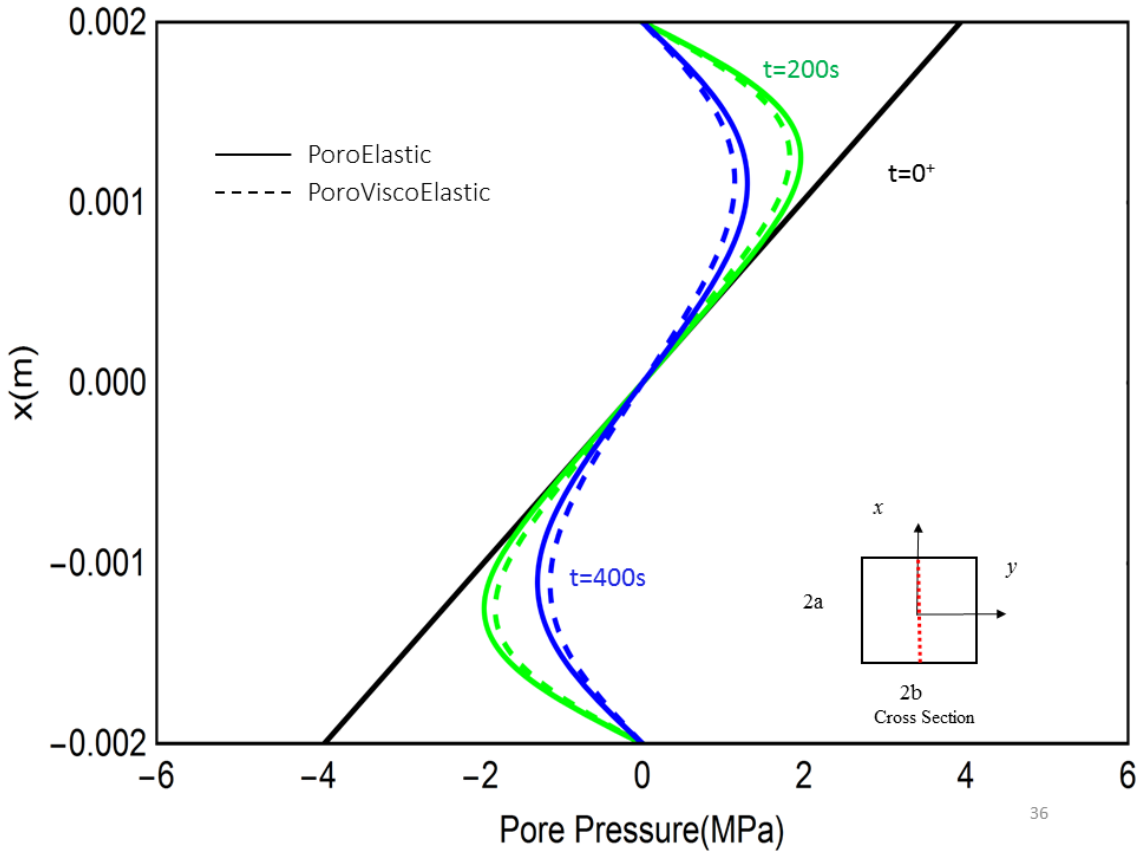


Figure 17. Poroelastic and poroviscoelastic pore pressure distribution along x-axis at y=0mm and z=40mm at variable times for transversely isotropic beam.

Figure 18 illustrates the pore pressure distribution along y-axis at x=1 mm and z= 40 mm. The initial pore pressure jump at $t=0^{+}$s is uniform along y-axis and this is the only time when the pore pressure at the boundary is bigger than 0. As time elapses and fluid flows out of the boundary, the pore pressure starts to drop and it is 0 at the boundary of the beam. Viscoelastic relaxation has the same effects on pore pressure along the y-axis as it does on that along the x-axis: it allows the pore pressure to drop faster. Also, the

overall decline rate of pore pressure slows down along with time.

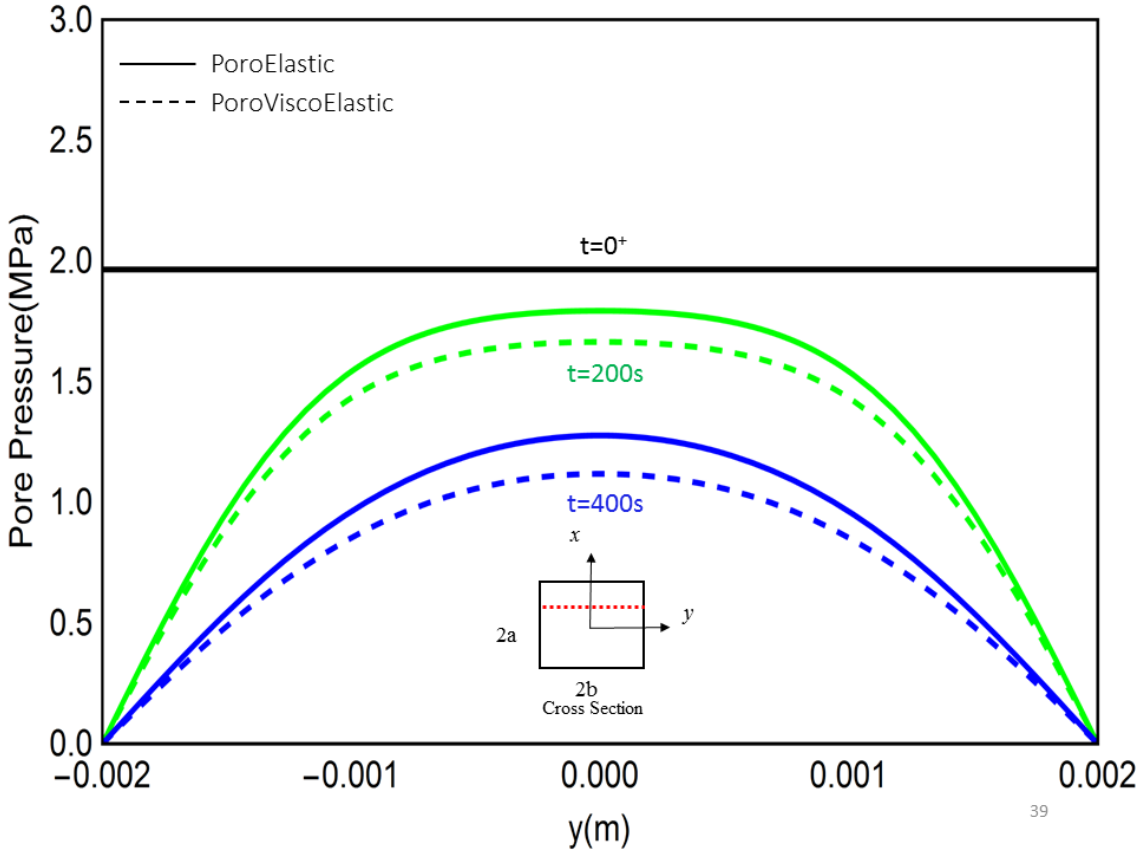


Figure 18. Poroelastic and poroviscoelastic pore pressure distribution along y-axis at x=1mm and z=40mm at variable times for transversely isotropic beam.

Figure 19 shows the load decay under constant deflection for a poroelastic and poroviscoelastic beam. For poroelastic case, the initial load at $t=0^{+}$ is equal to 11.9 N while at the end of the simulation t= 10, 000s, the load drops to 11.2 N. 11.2 N is reached at approximately t= 1, 000 s and this indicates the end of the hydrodynamic relaxation. At this point, the pore pressure has reached equilibrium under this deflection and equals to 0 Psi. Under this condition no fluid is flowing inside the beam. 11.2 N is therefore the load needed to sustain the constant deflection if the beam is elastic. From 11.9 N to 11.2 N, 5.8% reduction in load is observed for poroelastic beam. Once the beam is considered

as viscoelastic, the Young's Moduli will decrease with time following the viscoelastic model, in this case, Zener Model. Hydrodynamic relaxation as well as viscoelastic relaxation both contribute to the reduction of the load. Therefore, the load required to sustain the same deflection is smaller for the poroviscoelastic beam. However, the decay of the load is asymptotic to a certain value: 5.6 N in this case. The load will not decrease infinitely because the restriction from the Zener Model: as time goes to infinity, Young's Moduli will become less and less time-sensitive. At infinite time, the load required to sustain the poroviscoelastic beam at 1mm deflection is 5.6 N and this is a 53% reduction in load.

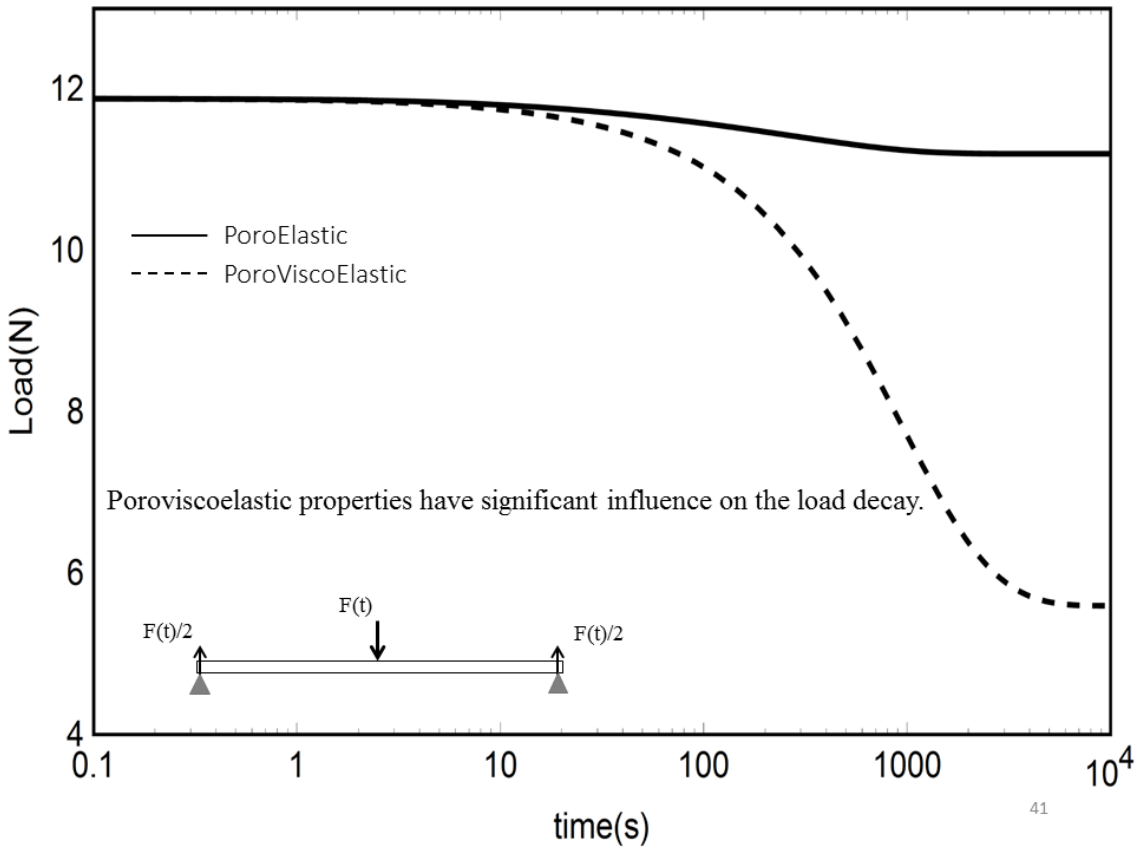


Figure 19. Poroelastic and poroviscoelastic load decay to sustain a 1mm constant deflection for transversely isotropic beam.

5.3 Effects of Various Shale Viscoelastic Behaviors

In this section, two models are used to simulate the viscoelastic properties of the beam: Zener Model and Sone-Zoback Model. Realistically shale is not an elastic material. Instead, shale would exhibit viscoelastic relaxation under load: Young's Moduli change with time. Both models simulate Young's Moduli as a function of time to capture the characteristic of the shale.

Zener Model:

$E(t) = E_0[1-\alpha+\alpha e^{-\frac{t}{\tau}}]$ with $\tau = 1000s$ and $\alpha = 0.5$

Sone-Zoback Model:

$E(t) = E_0 t^{-\beta}$ with $\beta = 0.008$

These two models generate a quite noticeable difference in load decay plots as represented in Figure 20. While the initial load is the same, the load under Zener model drops significantly faster than Sone-Zoback model, especially after 100s. However, due to the formula of Zener model, the load drops asymptotically when time goes to infinity. On the other hand, Sone-Zoback allows the load to drop continuously.

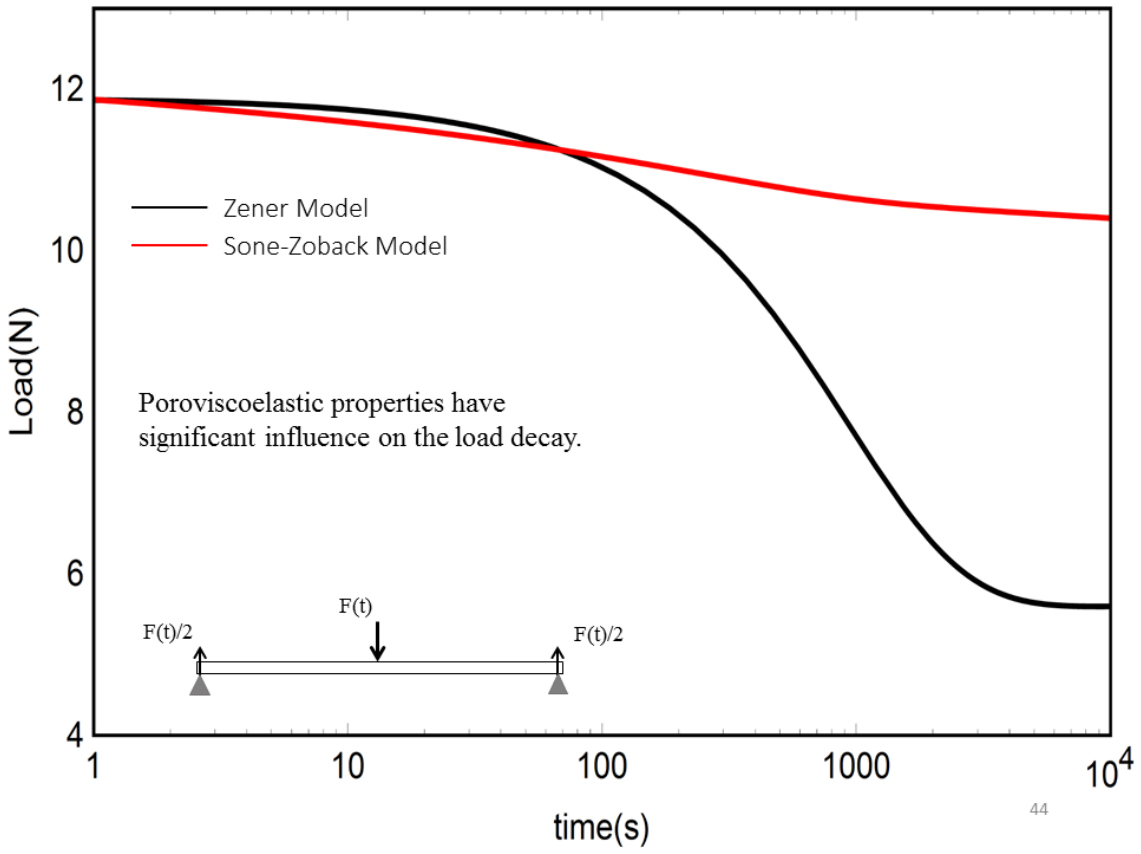


Figure 20. Poroviscoelastic load decay to sustain a 1mm constant deflection for orthotropic beams simulated by different viscoelastic models.

Chapter 6: Applications

6.1 Approximation of Shale Permeability

The most essential application of the three-point beam bending test is to estimate the permeability of the shale by matching the analytical solution of the load to the experimental data. Realistically, shale is conceivably viscoelastic: The Young's Moduli is time-dependent variable rather than a constant value. Therefore, selecting the correct viscoelastic model is crucial in generating an analytical solution which will match the data well. The author presents the following general steps (Figure 21) to recognize the viscoelastic models for shale from the experimental data.

To make sure essential information is obtained to determine the viscoelastic model for the shale, the experiment should go on for sufficient time that hydrodynamic relaxation has ended and all fluid inside the beam is drained, which means that the load decay is purely due to the viscoelastic relaxation.

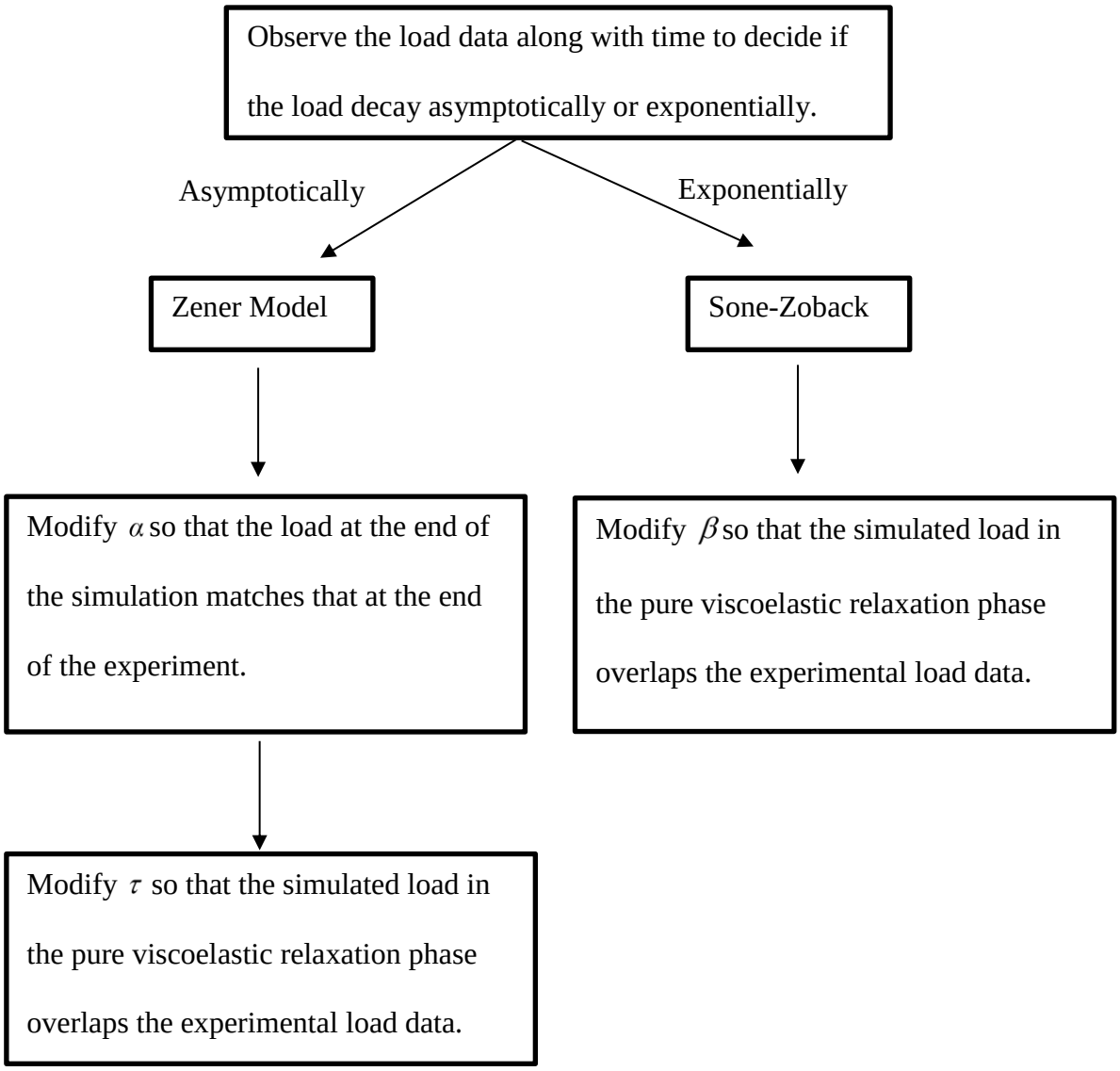


Figure 21. Simple work flow of determining which viscoelastic model to use based on the load decay data.

The most important part of adopting this procedure is to make sure that the experiment has gone on long enough into the pure viscoelastic relaxation phase after the hydrodynamic relaxation has ended. The viscoelastic model could only be made as close as possible if handful of load during viscoelastic relaxation phase is presented.

The experimental data of load decay of a transfer isotropic shale beam from Zhang and Scherer (2012) is adopted here to justify the validity of the method. Figure 22 shows the normalized load decay data along with time from a constant deflection three-point beam bending test. The beam has a dimension of 4mm by 4mm by 80mm and is placed in such an orientation that the isotropic plane is parallel to the load direction. The constant deflection is set to be 1mm at the center. The beam is sealed laterally in y and z direction; therefore, fluid is only allowed to flow in x-direction.

The mechanical properties of the shale and saturated fluid are provided by Zhang and Scherer(2012): porosity, $\phi = 3.5\%$, grain bulk modulus, $K_s = 40GPa$, initial Young's modulus in x-direction, y-direction, and z-direction are $E_x(0^+) = 30GPa$, $E_y(0^+) = 20GPa$ and $E_z(0^+) = 25GPa$ respectively. The saturated fluid is ethanol and has a bulk modulus of $K_f = 0.8GPa$ and fluid viscosity of $\mu = 0.001Pa \cdot s$.

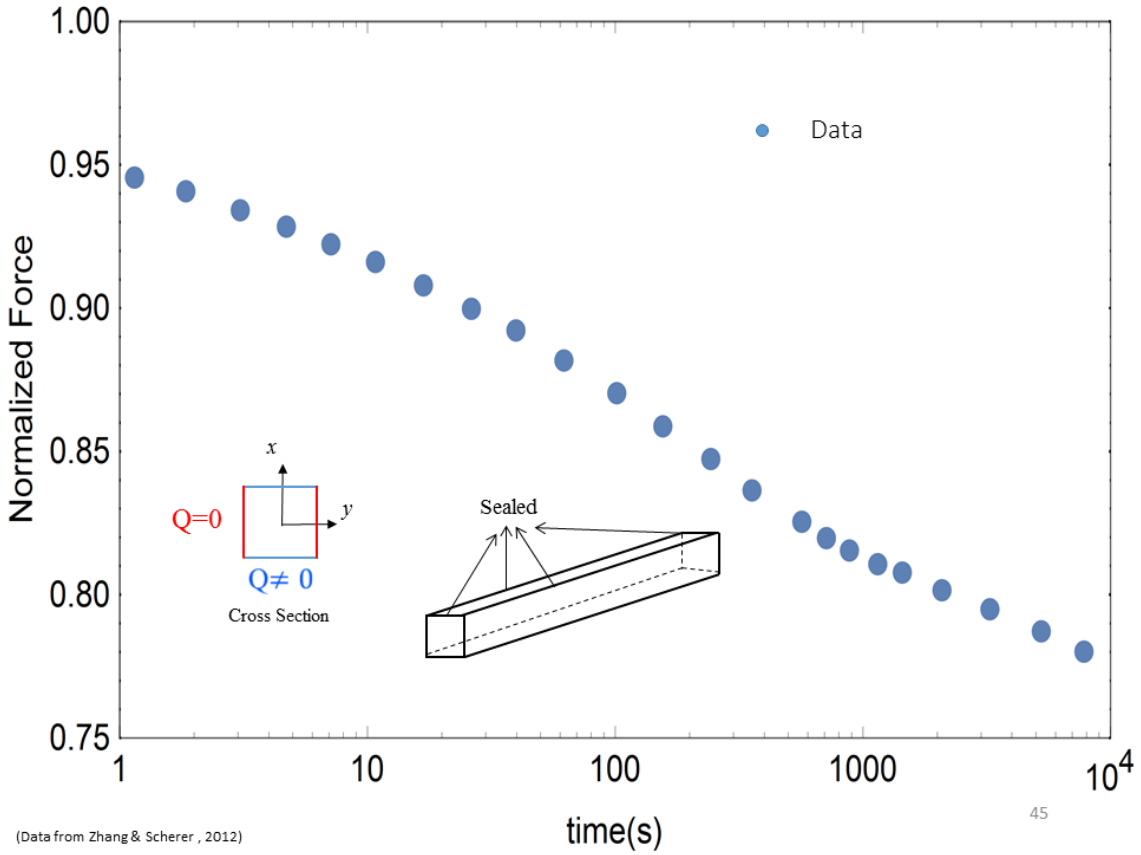


Figure 22. Experimental data of load decay of a shale under 1mm constant deflection three-point beam bending test.

By observing the load data, one could conclude that the Sone-Zoback model is more suitable for this shale and by modifying the viscoelastic parameter one can find $\beta = 0.02$. With the viscoelastic model and all the necessary data in hand, the author uses Mathematica to approximate the permeability: $k_x = 0.19nD$. The analytical solution generated by Mathematica is in great agreement with the load data as shown below:

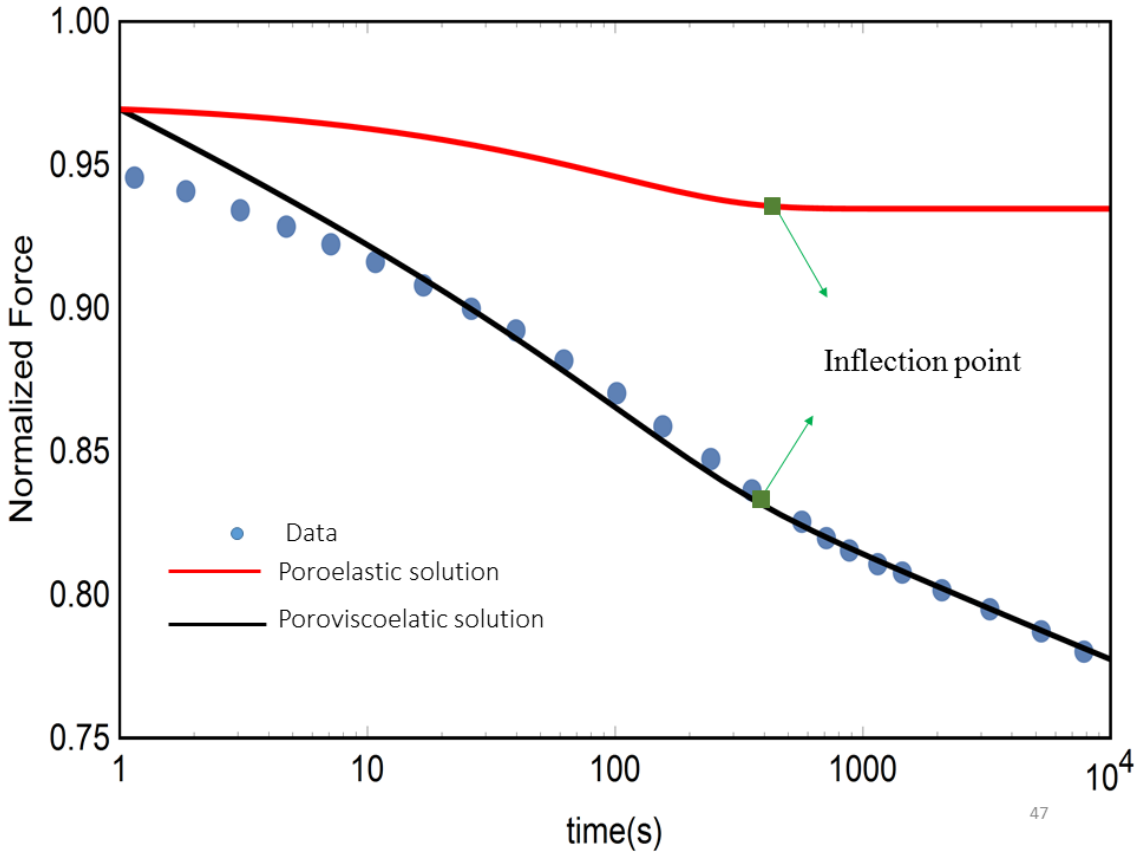


Figure 23. Matching the analytical solution of the poroviscoelastic load decay to the experimental data to obtain the estimated permeability.

Figure 23 includes the poroelastic and poroviscoelastic analytical solutions of the load decay. The inflection point in the poroviscoelastic load decay coincide with the minimum hydrodynamic relaxation point (the point where poroelastic load starts to stay flat). From this point onward, the load decay is almost purely caused by the viscoelasticity of the beam because the hydrodynamic relaxation can be neglected.

6.2 Sensitivity Studies

Sensitivity of the permeability on the load decay is studied as well and is shown in Figure 24. Permeability is modified to change in the magnitude of ten and compared

how the poroviscoelastic load would decay differently. As a result, the load would drop in quite different manners as permeability varies. Therefore, the solution is sensitive to the data and proves to be a reliable method to approximate permeability.

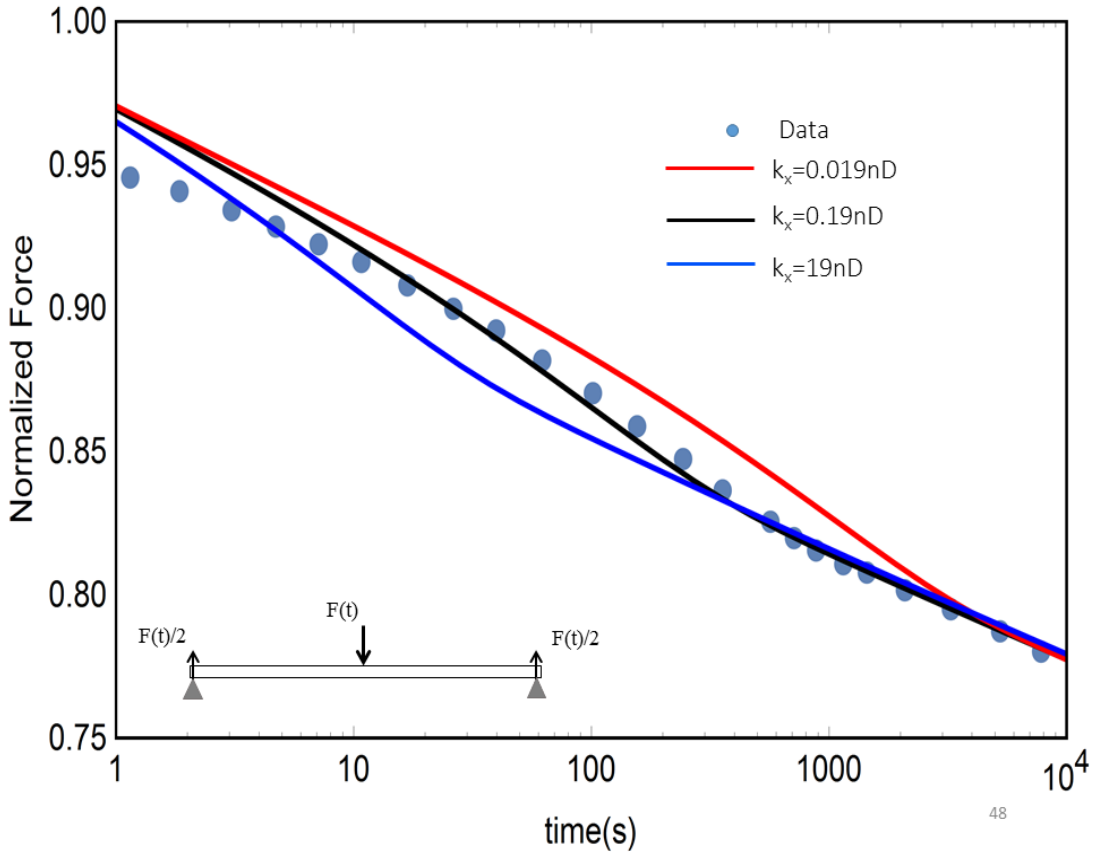


Figure 24. Poroviscoelastic load decay solutions with modified permeability

Effects of viscoelastic parameter β on load decay is investigated by modifying the value of it. β is modified based on the data given. Changing the value of β is an important step to generate the best match. Therefore, different values of β should be used when a different set of data is given. Figure 25 reveals the effects of various values of viscoelastic parameter β.

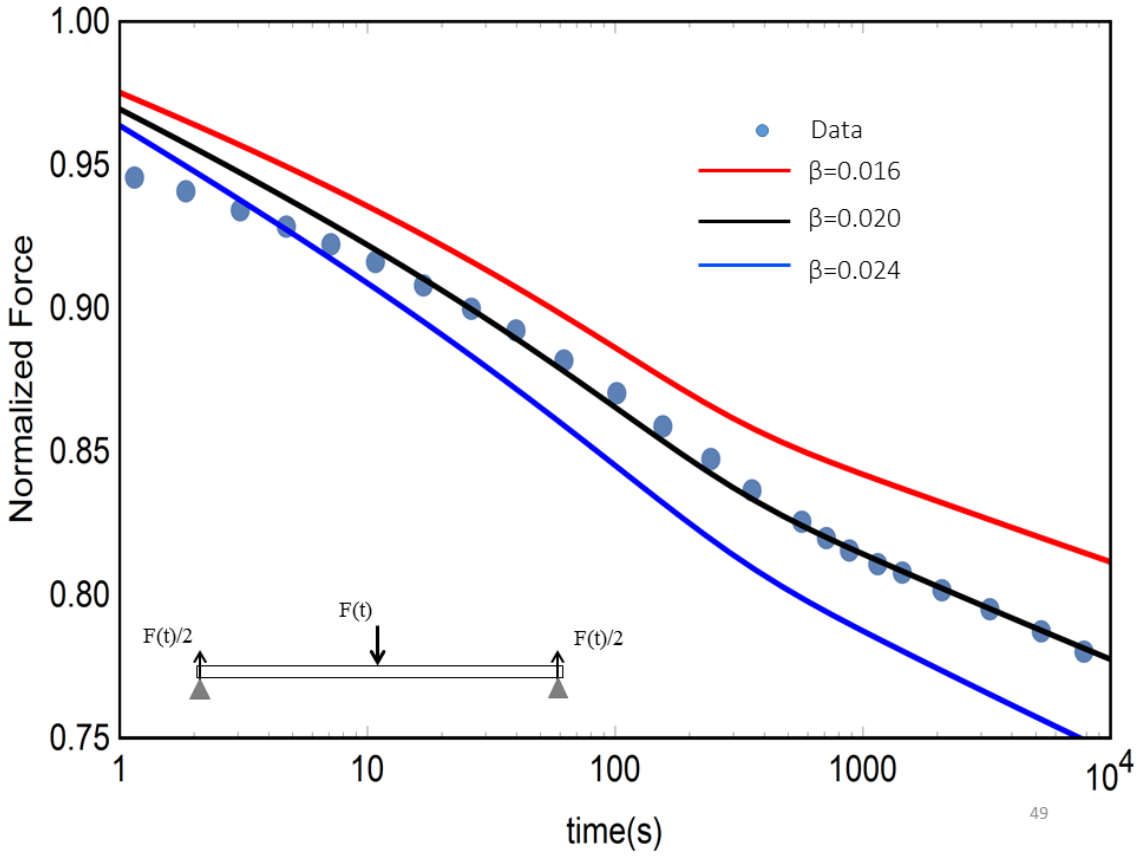


Figure 25. Poroviscoelastic load decay with modified viscoelastic parameter

6.3 Potential Improvement of the Test

One of the important steps during matching analytical solution of the poroviscoelastic load decay to the real measured data is to find a proper viscoelastic model to capture the viscoelasticity of the shale. Finding the right viscoelastic model could be a challenge since it is not easy to obtain the exact viscoelastic variables in the model when the load data is the only thing given. However, one may neglect the viscoelastic model and still approximate the permeability of the shale if he or she can get rid the viscoelastic effects and reduce the load decay to a poroelastic one.

To do so, one needs to perform an exact constant deflection three-point beam bending test on an exact same unsaturated shale beam. By doing so, the load decay data

would reflect pure viscoelastic relaxation. Then subtract the load decay caused by viscoelastic relaxation from the poroviscoelastic load decay obtained from a saturated shale beam. The remaining load decay would be solely due to the hydrodynamic relaxation. Thus, one could use the poroelastic solution of the load decay to match the data and approximate the permeability.

By successfully performing the three-point beam bending test on saturated and unsaturated samples manipulating the data, one could avoid coming up with a model to capture the viscoelasticity of the shale.

Ethanol is used as the fluid to saturate the rock in the experiment because shale experiences least swelling when ethanol is sued compared with other fluids. However, the practicality of ethanol as the saturation fluid in shale still needs to be justified since the molecular size of ethanol is big compared to pore throat size of shale: using ethanol may clog the small pores inside shales.

Finally, the fact that Darcy's law is used as the governing equations of fluid flow in porous media and the usage of it may not be applicable for shale. The flow of fluid in such extremely small pores of shale may not be completely captured when Darcy's Law is used as the fluid flow model. More complicated models need to be introduced to accurately simulate the flow.

Chapter 7: Conclusions

The work develops the orthotropic poroviscoelastic solutions to the three-point beam bending test. Factors which influence the pore pressure profile and the load decay for a constant deflection test are investigated: anisotropy, permeability, viscoelastic parameters and viscoelastic models. The author concludes that all these factors have significant influence on the load decay hence the permeability estimation. Therefore, holistic consideration of all the factors are important when a three-point beam bending test is performed.

Permeability of the shale is approximated from one set of data by fitting the analytical solution to the experimental data of load. The matching turns out to be a good agreement with the data and therefore the permeability and poroviscoelastic properties are successfully approximated.

Finding an adequate viscoelastic model to simulate the shale viscoelastic behavior and modifying it to fit the experimental data could be a tedious job. The author makes an assumption that by performing the three-point beam bending test on an unsaturated and saturated sample and manipulate the load decay data to cancel out the viscoelastic relaxation. Further experiments need to be done to test the validity of this assumption.

The author only tests one set of the data due to the shortage of experimental data in hand. The numerical examples are carried out to thoroughly study the test under different scenarios. Once more data are available, the analytical solutions derived from this work could be readily used.

References

Abousleiman, Y., Cheng, A., Jiang, C., and Roegiers, J. 1993. A micromechanically consistent poroviscoelasticity theory for rock mechanics applications. *International Journal of Rock Mechanics and Mining Sciences & Geomechanics Abstracts* **30**(7): 1177-1180. http://dx.doi.org/10.1016/0148-9062(93)90090-Z.

Abousleiman, Y., Cheng, A. H.-D., Cui, L., Detournay, E., and Roegiers. J.-C. 1996. Mandel's problem revisited: *Géotechnique*, **46**(2): 187-195. http://dx.doi.org/10.1680/geot.1996.46.2.187.

Abousleiman, Y., A. H.-D. Cheng, C. Jiang, and J.-C. Roegiers. 1996. Poroviscoelastic analysis of borehole and cylinder problems. *Acta Mechanica* **119**(1): 199-219. http://dx.doi.org/ 10.1007/BF01274248.

Abousleiman, Y., and L. Cui, 1998, Poroelastic Solutions in Transversely Isotropic Media for Wellbore and Cylinder. *International Journal of Solids and Structures*, **35**(34-35): 4905-4929. http://dx.doi.org/10.1016/S0020-7683(98)00101-2.

Abousleiman, Younane. and Cheng, A. H-D. 2005. Poromechanics – Biot Centennial (1905-2005), first edition, London: Taylor & Francis Group.

Abousleiman, Y. N., Hoang, S., and Liu, C. 2013, Anisotropic porothermoelastic solution and hydro-thermal effects on fracture width in hydraulic fracturing. *International Journal for Numerical and Analytical Methods in Geomechanics* **38**(5): 493-517. http://dx.doi.org/10.1002/nag.2216.

Abousleiman, Y., 2016, Mechanics of Materials: Stress-Strain Diagram [Powerpoint slides].

Abousleiman, Y., 2016, Mechanics of Materials: Bending [Powerpoint slides].

Almasoodi, M., Abousleiman, Y., and Hoang, Son. 2014. Viscoelastic Creep of Eagle Ford Shale: Investigating Fluid-Shale Interaction. Presented at SPE/CSUR Unconventional Resources Conference, Canada, 30 September – 2 October. SPE-171569-MS. http://dx.doi.org/10.2118/171569-MS.

Biot, M. A. 1941. General theory of three-dimensional consolidation. *Journal of Applied Physics* **12**(2): 155-164. http://dx.doi.org/10.1063/1.1712886.

Biot, M. A. 1955. Theory of Elasticity and Consolidation for a Porous Anisotropic Solid. *Journal of Applied Physics* **26**, 182–185. http://dx.doi.org/10.1063/1.1721956.

Bloch, M., Cui, L., Abousleiman, Y., and Roegiers, J. C. 1999. Poroviscoelastic Effects in Anelastic Strain Recovery Tests. Presented at the 37th US Symposium on Rock Mechanics, Vil, Colorado, 7-9 June. ARMA-99-1165.

Bloch, M. and Abousleiman, Y. 2000. Poroviscoelastic Solution for Anelastic Strain Recovery. Presented at the 40th North American Rock Mechanics Symposium, Seattle, Washington, 31 July – 3 August. ARMA-2000-0857.

Carslaw, H. S. and Jaeger, J. C. 1959. *Conduction of Heat in Solids*, second edition. London: Oxford University Press.

Cheng, A. H-D., Sidauruk, P., and Abousleiman, Y. 1994. Approximate Inversion of the Laplace Transform: *The Mathematica Journal* **4**(2): 76-82.

Christensen, R. M. 1980. A Nonlinear Theory of Viscoelasticity for Application to Elastomers. *Journal of Applied Mechanics* **47**(4): 762-768. http://dx.doi.org/10.1115/1.3153787.

Comisky, J.T., Newsham, K., Rushing, J.A., and Blashingame, T. A. 2007. A Comparative Study of Capillary-Pressure-Based Empirical Models for Estimating Absolute Permeability in Tight Gas Sands. Presented at the SPE Annual Technical Conference and Exhibition, Anaheim, 11-14 November. SPE-110050-MS. http://dx.doi.org/10.2118/110050-MS.

Crook, A., Yu, JG., and Willson, S.2002. Development of an Orthotropic 3D Elastoplastic Material Model for Shale. Presented at SPE/ISRM Rock Mechanics Conference, Irving, Texas, 20-23 October. SPE-78238-MS. http://dx.doi.org/10.2118/78238-MS.

Guo, J. X. 2015. Poroviscoelastic Anisotropy for Shale Permeability: Theory and Application: Master Thesis, University of Oklahoma.

Hoang, S. and Abousleiman, Y. 2009. Poroviscoelastic Two-Dimensional Anisotropic Solution with Application to Articular Cartilage Testing. *Journal of Engineering Mechanics* **135** (5): 367-374. http://dx.doi.org/10.1061/(ASCE)0733-9399(2009)135:5(367)

Hoang, S. and Abousleiman, Y. 2009. Critical Poroviscoelastic Anisotropic Evaluation of Anelastic Strain Recovery Test. Presented at SPE Annual Technical Conference and Exlahibition, New Orleans, Louisiana, 4-7 October. SPE-124330-MS. http://dx.doi.org/10.2118/124330-MS.

Hoang, S. K., and Y. N. Abousleiman. 2010. Poroviscoelasticity of transversely isotropic cylinders under laboratory loading conditions. *Mechanics Research Communications* **37** (3): 298-306. http://dx.doi.org/10.1016/j.mechrescom.2010.01.008.

Hoang, S. K., 2011, Poroviscoelasticity and Analytical Solutions of Selected Problems in Engineering: Ph. D. dissertation, University of Oklahoma.

Hoang, S. K., and Y. N. Abousleiman. 2012. Correspondence principle between anisotropic poroviscoelasticity and poroelasticity using micromechanics and application to compression of orthotropic rectangular strips: *Journal of Applied Physics* **112**(4):1-15. http://dx.doi.org/10.1063/1.4748293.

Hoang, S., Abousleiman, Y., and Hemphill, T. 2012. Poroviscoelastic Modeling of Time-Dependent Wellbore Closure when Drilling Anisotropic Gas Shale and Oil Shale Reservoirs - Applications in the Haynesville Shale and the Colony Pilot Mine Shale. Presented at SPE Annual Technical Conference and Exlahibition, San Antonio, Texas, 8-10 October. SPE-159942-MS.

Huang, J. and Ghassemi, A. 2013. Simulating Geomechanical Evolution of Fractured Shale Using a Poro-viscoelastic Constitutive Model. Presented at the 47th US Rock Mechanics/Geomechanics Symposium, San Francisco, California, 23-26 June. ARMA-2013-173.

Mehrabian, A. and Abousleiman, Y. 2011. General solutions to poroviscoelastic model of hydrocephalic human brain tissue. *Journal of Theoretical Biology* **291**: 105-118. http://dx.doi.org/10.1016/j.jtbi.2011.09.011.

Mehrabian, A., Abousleiman, Y., Mapstone, T., and El-Amm, C. 2015. Dual-porosity poroviscoelasticity and quantitative hydromechanical characterization of the brain tissue with experimental hydrocephalus data. *J Theor Biol* **384**: 19-32. http://dx.doi.org/10.1016/j.jtbi.2015.08.001.

Nguyen, V. X., 2010, Dual-Porosity and Dual-Permeability Poromechanics Solutions for Problems in Laboratory and Field Applications: Ph.D. Dissertation, University of Oklahoma.

Sargand, S. M. and Hazen, G. A. 1987. Technical Note: Deformation Behavior of Shales. *Int. J. Rock Mech. Min. Sci & Geomech. Abstr*. **24** (6): 365-370.

Scherer, G. W. 1992. Bending of gel beams: method for characterizing elastic properties and permeability. *Journal of Non-Crystalline Solids*, **142**: 18–35. http://dx.doi.org/10.1016/S0022-3093(05)80003-1.

Scherer, G. W. 1994. Relaxation of a viscoelastic Gel Bar: I. Theory. *Journal of Sol-Gel Science and Technology* **1**(2): 169-175. http://dx.doi.org/10.1007/BF00490246.

Scherer, G. W. 1994. Stress in Aerogel During Depressurization of Autoclave: I. Theory. *Journal of Sol-Gel Science and Technology* **3**(2): 127-139. http://dx.doi.org/10.1007/BF00486719.

Scherer, G. W. 2000. Measuring permeability of rigid materials by a beam-bending method: I, theory. *Journal of the American Ceramic Society* **83** (9): 2231–2239. http://dx.doi.org/10.1111/j.1151-2916.2000.tb01540.x.

Scherer, G. W. 2004. Measuring permeability of rigid materials by a beam-bending method: IV, transversely isotropic plate. *Journal of the American Ceramic Society* **87**(8): 1517–1524.

Sone, H., 2012. Mechanical properties of shale gas reservoir rocks and its relation to the in-situ stress variation observed in shale gas reservoirs: Ph.D. dissertation, Stanford University.

Valenza, John and Scherer, G. W. 2004. Measuring permeability of rigid materials by a beam-bending method: V, Isotropic Rectangular Plates of Cement Paste. *Journal of the American Ceramic Society* **87**(10): 1927-1931. http://dx.doi.org/10.1111/j.1151-2916.2004.tb06342.x.

Wang, Z. H., Prevost, J. H., and Coussy, O. 2009. Bending of fluid saturated linear poroelastic beams with compressible constituents. *International Journal for Numerical and Analytical Methods in Geomechanics* **33**: 425-447. http://dx.doi.org/10.1002/nag.722.

Zhang, J., and Scherer, G. W. 2012. Permeability of shale by the beam-bending method. *International Journal of Rock Mechanics and Mining Sciences*, **53**: 179-191. http://dx.doi.org/10.1016/j.ijrmms.2012.05.011.

Appendix A: Derivation of the Instantaneous Pore Pressure Jump

$$\sigma_{xx} = M_{11}\varepsilon_{xx} + M_{12}\varepsilon_{yy} + M_{13}\varepsilon_{zz} + \alpha_1 p \tag{A.1}$$

$$\sigma_{yy} = M_{12}\varepsilon_{xx} + M_{22}\varepsilon_{yy} + M_{23}\varepsilon_{zz} + \alpha_2 p \tag{A.2}$$

$$\sigma_{zz} = M_{13}\varepsilon_{xx} + M_{23}\varepsilon_{yy} + M_{33}\varepsilon_{zz} + \alpha_3 p \tag{A.3}$$

$$p = M(\alpha_1\varepsilon_{xx} + \alpha_2\varepsilon_{yy} + \alpha_3\varepsilon_{zz} + \zeta) \tag{A.4}$$

Under constant deflection, $\sigma_{xx} = \sigma_{yy} = 0$, therefore from B.1 and B.2

$$\varepsilon_{xx} = \frac{(M_{13}M_{22} - M_{23}M_{12})\varepsilon_{zz} + (\alpha_1 M_{22} - \alpha_2 M_{12})p}{M_{12}M_{12} - M_{11}M_{22}} \tag{A.5}$$

$$\varepsilon_{yy} = \frac{(M_{13}M_{12} - M_{23}M_{11})\varepsilon_{zz} + (\alpha_1 M_{12} - \alpha_2 M_{11})p}{M_{11}M_{22} - M_{12}M_{12}} \tag{A.6}$$

Substitute B.5 and B.6 into B.4 and express ζ:

$$\zeta = \left(\frac{1}{M} - \frac{\alpha_1(\alpha_1 M_{22} - \alpha_2 M_{12}) - \alpha_2(\alpha_1 M_{12} - \alpha_2 M_{11})}{M_{12}M_{12} - M_{11}M_{22}}\right)p - \left(\frac{\alpha_1(M_{13}M_{22} - M_{23}M_{12}) - \alpha_2(M_{13}M_{12} - M_{23}M_{11})}{M_{12}M_{12} - M_{11}M_{22}} + \alpha_3\right)\varepsilon_{zz} \tag{A.7}$$

Fluid flow is governed by Darcy's law:

$q_i = -\frac{k_i}{\mu}\frac{\partial p}{\partial i}$ (B.8) where $i = x, y$ since we neglect flow in z-direction

Mass balance equation:

$$\frac{\partial \zeta}{\partial t} + \frac{\partial q_i}{\partial i} = 0 \tag{A.8}$$

Substitute B.7 and B.8 into B.9 with the knowledge that $\frac{\partial \varepsilon_{zz}}{\partial t} = 0$ because flow in z-direction is assumed to be 0:

$$\left(\frac{1}{M} - \frac{\alpha_1(\alpha_1 M_{22} - \alpha_2 M_{12}) - \alpha_2(\alpha_1 M_{12} - \alpha_2 M_{11})}{M_{12}M_{12} - M_{11}M_{22}}\right)\frac{\partial p}{\partial t} = \frac{k_x}{\mu}\frac{\partial^2 p}{\partial x^2} + \frac{k_y}{\mu}\frac{\partial^2 p}{\partial y^2} \tag{A.9}$$

After normalizing the time and location coordinates and rearranging, the following term is obtained:

$$\frac{\partial p}{\partial \theta} = \frac{\partial^2 p}{\partial v^2} + \kappa \frac{\partial^2 p}{\partial w^2} \tag{A.10}$$

Where $\theta = t/\tau$ with $\tau = \dfrac{(\frac{1}{M} - \frac{\alpha_1(\alpha_1 M_{22} - \alpha_2 M_{12}) - \alpha_2(\alpha_1 M_{12} - \alpha_2 M_{11})}{M_{12}M_{12} - M_{11}M_{22}})\mu a^2}{k_x}$, $v = x/a$

, $w = y/b$ with 2a and 2b the depth and width of the beam cross section and $\kappa = \dfrac{a^2 k_y}{b^2 k_x}$.

Substitute B.5 and B.6 into B.4 and rearrange:

$$(\frac{1}{M} - \frac{\alpha_1(\alpha_1 M_{22} - \alpha_2 M_{12})}{M_{12}M_{12} - M_{11}M_{22}} + \frac{\alpha_2(\alpha_1 M_{12} - \alpha_2 M_{11})}{M_{12}M_{12} - M_{11}M_{22}})p = (\frac{\alpha_1(M_{13}M_{22} - M_{23}M_{12})}{M_{12}M_{12} - M_{11}M_{22}} - \frac{\alpha_2(M_{13}M_{12} - M_{23}M_{11})}{M_{12}M_{12} - M_{11}M_{22}} + \alpha_3)\varepsilon_{zz} + \zeta \tag{A.11}$$

Axial strain (independent of time) can be expressed as (Scherer 1992):

$$\varepsilon_{zz} = \frac{24\Delta xz}{L^3} = \frac{24\Delta az}{L^3} v \tag{A.12}$$

Where Δ is the deflection.

When the deflection is instantaneously applied, the fluid is not flowing out of the matrix therefore in B.12 $\zeta_0 = 0$ (the subscript 0 indicates an initial value). Substitute B.13 into B.12 the initial pore pressure P_0 is derived as:

$$p_0 = 24\frac{\dfrac{\alpha_1(M_{13}M_{22}-M_{23}M_{12})}{M_{12}M_{12}-M_{11}M_{22}} - \dfrac{\alpha_2(M_{13}M_{12}-M_{23}M_{11})}{M_{12}M_{12}-M_{11}M_{22}} + \alpha_3}{\dfrac{1}{M} - \dfrac{\alpha_1(\alpha_1 M_{22}-\alpha_2 M_{12})}{M_{12}M_{12}-M_{11}M_{22}} + \dfrac{\alpha_2(\alpha_1 M_{12}-\alpha_2 M_{11})}{M_{12}M_{12}-M_{11}M_{22}}}\frac{\Delta a}{L^3} z\nu = p_{00}\nu \qquad \text{(A.13)}$$

where $$p_{00} = 24\frac{\dfrac{\alpha_1(M_{13}M_{22}-M_{23}M_{12})}{M_{12}M_{12}-M_{11}M_{22}} - \dfrac{\alpha_2(M_{13}M_{12}-M_{23}M_{11})}{M_{12}M_{12}-M_{11}M_{22}} + \alpha_3}{\dfrac{1}{M} - \dfrac{\alpha_1(\alpha_1 M_{22}-\alpha_2 M_{12})}{M_{12}M_{12}-M_{11}M_{22}} + \dfrac{\alpha_2(\alpha_1 M_{12}-\alpha_2 M_{11})}{M_{12}M_{12}-M_{11}M_{22}}}\frac{\Delta a}{L^3} z \qquad \text{(A.14)}$$

Appendix B: Poroelastic Solutions for Pore Pressure

The partial differential equation and its boundary and initial conditions are as follows:

PDE:

$$\frac{\partial P}{\partial \theta} = \frac{\partial^2 P}{\partial v^2} + \kappa \frac{\partial^2 P}{\partial w^2} \tag{B.1}$$

BC:

$$P(\pm 1, w, \theta) = P(v, \pm 1, \theta) = 0 \tag{B.2}$$

IC:

$$p(v, w, 0) = p_0 v \tag{B.3}$$

where p_0 is a linear function of z and is derived in Appendix B.

Solutions:

Step 1: separation of variables:

$$p(v, w, \theta) = p_1(v, w)\, p_2(\theta) \tag{B.4}$$

Substitute into Eq. A.1, divide both sides by $p_1 p_2$ and rearrange:

$$\frac{dP_2}{d\theta} \Big/ p_2 = \frac{\partial^2 P_1}{\partial v^2} \Big/ p_1 + \kappa \frac{\partial^2 P_1}{\partial w^2} \Big/ p_1 = -\lambda \tag{B.5}$$

The left-hand side is a function of p_2 and right hand side p_1. Therefore, the equation is equal to a constant namely $-\lambda$.

Now two new PDEs are obtained:

$$\frac{\partial^2 P_1}{\partial v^2} \Big/ p_1 + \kappa \frac{\partial^2 P_1}{\partial w^2} \Big/ p_1 = -\lambda \tag{B.6a}$$

$$\frac{dP_2}{d\theta} \Big/ p_2 = -\lambda \tag{B.6b}$$

Apply separation of variables on p_1

$$p_1 = f(v)g(w) \tag{B.7}$$

Substitute back to A.6 and rearrange:

$$\frac{f''}{f} = -\lambda - \frac{\kappa g''}{g} = -\omega \tag{B.8a}$$

$$\frac{f''}{f} = -\omega \tag{B.8b}$$

$$\frac{g''}{g} = -\frac{\lambda - \omega}{\kappa} \tag{B.8c}$$

Where $-\omega$ is a constant since two sides of the equality are independent of each other in A.8a.

Step 2: Solving ODEs:

Solving the $p_2(\theta)$ from A.6b:

$$p_2(\theta) = Ce^{-\lambda\theta} \tag{B.9}$$

Where C is a constant.

Move on to solve Eq. A.8:

We are aware of that pore pressure solution behaves like trigonometric functions therefore $\omega > 0$ and $\frac{\lambda - \omega}{\kappa} > 0$ the solutions to $f(v)$ and $g(\theta)$ from A.8 are as follows:

$$f = a_1 \cos\sqrt{\omega}v + a_2 \sin\sqrt{\omega}v \tag{B.10a}$$

$$g = a_3 \cos\sqrt{\tfrac{\lambda-\omega}{\kappa}}w + a_4 \sin\sqrt{\tfrac{\lambda-\omega}{\kappa}}w \tag{B.10b}$$

Where $a_1\ a_2\ a_3\ a_4$ are constants.

The boundary conditions A.2 can be decomposed as boundary conditions for $f(v)$ as follows:

$$f(1) = a_1 \cos\sqrt{\omega} + a_2 \sin\sqrt{\omega} = 0 \quad \text{(B.11a)}$$

$$f(-1) = -a_1 \cos\sqrt{\omega} - a_2 \sin\sqrt{\omega} = 0 \quad \text{(B.11b)}$$

Two cases are obtained from the above boundary conditions:

Case 1: $f = \sin m\pi v$ where $m = 1.2.3....$ with $\omega = m^2\pi^2$ (B.12a)

Case 2: $f = \cos\frac{(2m-1)\pi}{2} v$ where $m = 1.2.3....$with $\omega = (\frac{(2m-1)\pi}{2})^2$ (B.12b)

Similarly, two cases from the boundary conditions A.2 for $g(w)$ are obtained:

Case 1: $g = \sin n\pi v$ where $n = 1.2.3....$ with $\frac{\lambda - \omega}{\kappa} = n^2\pi^2$ (B.13a)

Case 2: $g = \cos\frac{(2n-1)\pi}{2} v$ where $n = 1.2.3....$with $\frac{\lambda - \omega}{\kappa} = (\frac{(2n-1)\pi}{2})^2$ (B.13b)

From A13-A14:

$$\lambda = \kappa(\frac{(2n-1)\pi}{2})^2 + m^2\pi^2 \quad \text{(B.14)}$$

Therefore A.9 becomes:

$$p_2(\theta) = Ce^{-[\kappa(\frac{(2n-1)\pi}{2})^2 + m^2\pi^2]\theta} \quad \text{(B.15)}$$

The initial condition A.3 can be decomposed as initial condition for P_1 and P_2 as follows:

$$p(v,w,0) = p_1(v,w)\,p_2(0) = f(v)g(w)h(0) = f(v)g(w) = p_0 v \quad \text{(B.16)}$$

The v term in initial condition A.15 must come from $f(v)$ hence $g(w)$ is a constant. Therefore, $f(v)$ is in the form of summation of sin functions (A.13a) and $g(w)$ is in the form of summation of cos functions(A.14b) (Carslaw, H. S. and Jaeger, J. C. 1959).

Hence $f(v)$ and $g(w)$ will take the form of:

$$f(v) = -2p_0 \sum_{m=1}^{\infty} \frac{(-1)^m}{a_m} \sin a_m v \quad \text{(B.17)}$$

$$g(w) = -2\sum_{n=1}^{\infty} \frac{(-1)^n}{b_n} \cos b_n w \tag{B.18}$$

Where $a_m = m\pi$ and $b_n = \frac{(2n-1)\pi}{2}$ with $m, n \in N$

The solution is the product of A. and A. after applying principle of superposition:

$$p = 4p_0 \sum_{m=1}^{\infty} \sum_{n=1}^{\infty} \frac{(-1)^m}{a_m} \frac{(-1)^n}{b_n} \sin(a_m v) \cos(b_n w) e^{-(\kappa b_n^2 + a_m^2)\theta} \tag{B.19}$$

Appendix C: Poroelastic Solutions for Moment and Load

Substitute B.5 and B.6 into B.3, σ_{zz} can be expressed as:

$$\sigma_{zz} = [\frac{M_{13}(M_{13}M_{22} - M_{23}M_{12}) - M_{23}(M_{13}M_{12} - M_{23}M_{11})}{M_{12}M_{12} - M_{11}M_{22}} + M_{33}]\varepsilon_{zz} + [\frac{M_{13}(\alpha_1 M_{22} - \alpha_2 M_{12}) - M_{23}(\alpha_1 M_{12} - \alpha_2 M_{11})}{M_{12}M_{12} - M_{11}M_{22}} + \alpha_3]p$$

(C.1)

where $\varepsilon_{zz} = \frac{24\Delta xz}{L^3}$ from Eq. B.13.

Moment at the cross section of the beam is expressed as $M_z = \int_A \sigma_{zz} x dA$ and therefore becomes:

$$M_z = [\frac{M_{13}(M_{13}M_{22} - M_{23}M_{12}) - M_{23}(M_{13}M_{12} - M_{23}M_{11})}{M_{12}M_{12} - M_{11}M_{22}} + M_{33}]\frac{24\Delta z}{L^3} I + [\frac{M_{13}(\alpha_1 M_{22} - \alpha_2 M_{12}) - M_{23}(\alpha_1 M_{12} - \alpha_2 M_{11})}{M_{12}M_{12} - M_{11}M_{22}} + \alpha_3]\int_A pxdA$$

(C.2)

where $I = \frac{4ba^3}{3}$ is the moment of inertia.

Pore pressure moment at the cross section of the beam is expressed as $M_p = \int_A pxdA$

After the integration:

$$\int_A pxdA = 4p_0 \sum_{m=1}^{\infty}\sum_{n=1}^{\infty} - \frac{4\times(-1)^{m+n} a^2 be^{-\theta(a_n^2 + b_m^2\kappa)}(a_n Cos[a_n] - Sin[a_n]Sin[b_m])}{a_n^3 b_m^2}$$

(C.3)

Where $\theta = t/\tau$ with $\tau = \frac{(\frac{1}{M} - \frac{\alpha_1(\alpha_1 M_{22} - \alpha_2 M_{12}) - \alpha_2(\alpha_1 M_{12} - \alpha_2 M_{11})}{M_{12}M_{12} - M_{11}M_{22}})\mu a^2}{k_x}$, with 2a and 2b the depth and width of the beam cross section and $\kappa = \frac{a^2 k_y}{b^2 k_x}$.

The load is related to moment by the following equation:

$$M_z(x) = \frac{F}{2}x \tag{C.4}$$

Therefore, $F = \frac{2M_z(x)}{x}$ (C.5)

